Chapter 3
Designed Magnetic Nanostructures

A. Enders, R. Skomski, and D.J. Sellmyer

Abstract The fabrication, structure, and magnetism of a variety of designed nanostructures are reviewed, from self-assembled thin-film structures and magnetic surface alloys to core–shell nanoparticles and clusters embedded in bulk matrices. The integration of clusters and other nanoscale building blocks in complex two- and three-dimensional nanostructures leads to new physics and new applications. Some explicitly discussed examples are interactions of surface-supported or embedded impurities and clusters, the behavior of quantum states in free and embedded clusters, the preasymptotic coupling of transition-metal dots through substrates, inverted hysteresis loops (proteresis) in core–shell nanoparticles, and nanoscale entanglement of anisotropic magnetic nanodots for future quantum information processing.

3.1 Introduction

Magnetic nanostructures form a broad range of geometries, chemical compositions, and internal structures, with intriguing physical properties and important applications [1–6]. Aside from thin films and multilayers, which are often considered as a separate field, there are natural or artificial dots, antidots, wires, and rings. Some examples of more complex nanostructures are core–shell particles [7, 8], including encapsulated transition-metal atoms or cluster-assembled solids such as $CrSi_{12}$ [9], various types of thin films [5, 10–16], doped clusters [17], and nanotubes [18]. Some bulk magnets may also be considered as embedded nanostructures, as exemplified by Sm–Co permanent magnets [3, 19, 20]. The structural features are on length scales ranging from less than 1 nm to several 100 nm [3, 18], and the involved magnetic substances range from magnetic elements (Fe, Co, Ni) and alloys (such as

A. Enders (✉)
Department of Physics and Astronomy and Nebraska Center for Materials and Nanoscience, University of Nebraska, Lincoln, NE 68508, USA
e-mail: axel@unl.edu

J.P. Liu et al. (eds.), *Nanoscale Magnetic Materials and Applications*,
DOI 10.1007/978-0-387-85600-1_3,

permalloy, $L1_0$ alloys, and rare-earth transition-metal intermetallics) to oxides and complicated compounds.

Non-interacting structures are interesting research subjects [21] and have important applications. For example, FePt nanoparticles with sizes down to 3 nm are of interest in permanent magnetism [22] but require coating by a thin shell or embedding in a matrix. A large volume fraction of the particles is necessary, because, the key figure of merit in permanent magnetism is the energy product, which scales as the square of the saturation magnetization $M_s = m/V$ in sufficiently hard magnets [23]. Another example is catalysis, which is usually realized by non-magnetic transition-metal surfaces [7]. The catalytic activity of a material [24] reflects subtle details of the electronic structure, which is easily modified by nanostructuring [25]. The confinement of electrons on a length scale of the order of 10 nm makes the electronic band-structure quasi-continuous, with level spacings and shifts sufficiently large to potentially interfere with the catalytic performance or the magnetic properties [26]. Other applications involving non-interacting nanoparticles are in optics, biomedicine [27], and magnetic recording (bit-patterned media) [28]. In the last case, a high-areal density of magnetic elements is required, and the suppression or management of the inter-particle interactions is an important, yet nontrivial task [4, 16, 29]. Figure 3.1 shows some elementary nanostructures, which can be produced in various homogeneous and inhomogeneous chemical compositions.

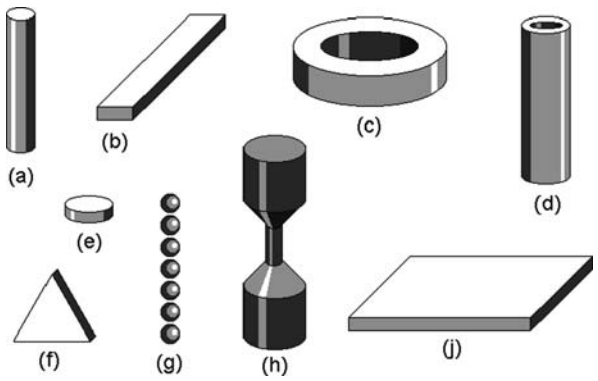

Fig. 3.1 This cartoon shows some simple nanostructures: (**a,b**) nanowires, (**c**) nanorings, (**d**) nanotube, (**e,f**) nanoparticles, (**g**) nanoparticle chain, (**h**) nanojunction, and (**j**) thin film. Chains of magnetite nanoparticles (**g**) naturally occur in the brains of animal such as bees and doves, where they may contribute to the spatial orientation during migration

The magnetic properties of the nanostructures in Fig. 3.1 are strongly influenced by their particular shape. But if the size of a metallic structure is decreased to only a few nanometers, then coordination effects become observable and exploitable. The reduced coordination results in an electronic structure different from that of bulk or single atoms. Fundamental magnetic properties, such as spin and orbital moments or magnetic anisotropy, are thus found to depend on the sample size and shape. For instance, clusters of Fe, Ni and Co in the gas phase show enhanced magnetic

moments per atom [30, 31], the magnetic anisotropy of clusters strongly depends on the number of atoms forming it [32, 33], and a magnetic moment is found in ultrathin layers of Rh, which is non-magnetic in the bulk [34]. But not only new magnetic and electronic properties emerge; also the structure [35], the reactivity [36] or thermal properties can deviate drastically from bulk behavior.

For surface-supported or embedded nanostructures, the mere size and shape are only among many other quantities that determine their properties. Also, mutual interactions [37], interactions with the substrate [38] or with ligands, capping layers, etc. influence their magnetic and electronic behavior, offering a wealth of possibilities to manipulate their magnetic properties. The desire emerges to use them in future devices such as patterned storage media, calling for the further study of nanoscale clusters deposited on surfaces. First experiments addressing the magnetic and structural cluster properties after deposition have been performed with rather large clusters consisting of $N > 100$ atoms [39, 40]. It turns out that size effects in the spin and orbital magnetic moments or the anisotropy energy become only observable in clusters of a few atoms in size. In fact, nanomagnetism is intermediate between atomic-scale magnetism and macroscopic magnetism (Maxwell′s equations) but cannot be considered as a superposition of the two limits [3]. Not only the size but also their areal density [41], the interaction with the substrate or a cover layer [42, 43], and the electronic exchange and hybridization during alloy formation decisively determine the magnetic cluster properties.

One aspect of the quest for new structures, new physics, and new applications is the development of *complex* nanostructures. Such structures can be used for logic operations [44, 45], exchange spring and other composite media for magnetic recording [23, 46–53], multiferroics [54], and can be rather exotic, such as three-dimensional arrays and hybrids involving living cells and magnetic nanostructures. The ultimate goal is the creation of complicated three-dimensional objects from nanoscale building blocks, and the hope is that complex structure and chemical composition results in complex interactions, and ultimately in useful properties or additional functionality. The achievable level of complexity of nanostructures depends on advances in fabrication and synthesis [55]. Intriguingly, new structures are often discovered in other areas of nanotechnology [56] but then develop into magnetic structures with very different physical properties, such as magnetic nanotubes [18].

The length scales considered in this review range from less than 1 nm to several 100 nm, although is in most cases the feature size are 5–20 nm. A natural length scale is $a_o/\alpha = 7.2$ nm [3, 57, 58], where a is Bohr's hydrogen radius and $\alpha = 1/137$ is Sommerfeld's fine-structure constant. Basically, this length scale determines the range of magnetic interactions and distinguishes nanostructures from macroscopic magnets.

The thermal stability of the magnetization direction in nanostructures is a critical for applications as magnetic recording media [46, 59]. For a small particle of volume V and anisotropy K, the relaxation time $\tau = \tau_o \exp(KV/k_B T)$, where $\tau_o \sim 10^{-10}$ s. The particle volume is usually limited, so that room temperature thermal stability requires the control and enhancement of the anisotropy, including surface and

interface anisotropy contributions [3]. Quantum-mechanical effects such as entanglement are even more demanding and require temperatures of 4.2 K or below. Thermally stable hard-magnetic nanoparticles can now be produced down to 3 nm [22], but some of the other nanostructures discussed here are of the low-temperature type.

In this chapter, we review synthesis strategies with prospect of success for the fabrication of moderately complex nanometer- and sub-nanometer scale structures and discuss relevant interactions and effects that determine the magnetic behavior of such structures as a result of their complexity.

3.2 Structure, Chemistry, and Geometry

Some nanostructures occur naturally—in minerals and biological systems—or are easily produced by bulk-processing methods. However, in most cases the structures are produced artificially, by using methods such as pulsed laser deposition (PLD), cluster deposition [60, 64], lithography [5], patterning using nanomasks and templates such as porous alumina [61], focused ion-beam milling (FIB) [45, 62], molecular-beam epitaxy (MBE), ball milling, STM deposition [63], melt spinning, lithography, and chemical vapor deposition (CVD). More recently, supramolecular chemistry [66] and self-assembly [65] have attracted special attention, as they allow for the fabrication of complex surface-supported structures with nearly atomic precision.

There is a crucial distinction between top-down and bottom-up methods. Top-down methods start from relatively big structural units and use methods such as cutting and milling to *decrease* the structure size. Examples of top-down methods are traditional microfabrication and lithography. By contrast, bottom-up methods start from very small units like atoms, molecules, or small clusters and implement concepts such as self-assembly and 'lock-and-key' type molecular recognition, with the goal to *increase* the structure size. It is anticipated that devices based on functional self-assembled structures will become available by combining both top-down and bottom-up fabrication steps [55]. A summary of all available techniques would go far beyond the scope of this chapter, but a few methods will be described as we go along.

The processing, analysis, or application of nanostructures requires their deposition on a surface, embedding in a matrix (Fig. 3.2), or incorporation into a more complicated structure (Fig. 3.3). Nanoscale embedding is characterized by interface-specific features that go beyond the short-range atomic order observed in many intermetallic compounds. The collective ferromagnetic behavior of Fe nanodots on Cu surfaces [38] or the canted uniaxial anisotropy of Fe or Co atoms at Pt step edges [67, 68] is direct consequences of embedding, i.e., the interaction of the nanostructure with the supporting host. A counter-example is rare-earth transition-metal alloys, where the relatively big rare-earth atoms tend to be surrounded by a large number of transition-metal atoms. These groups of atoms look like clusters—and some properties, such as the rare-earth anisotropy, can be interpreted as cluster

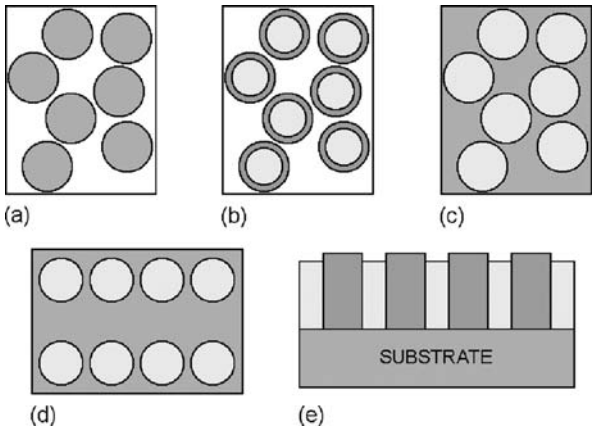

Fig. 3.2 Some types of embedding: (**a**) free isolated clusters, (**b**) free coated clusters, (**c**) randomly distributed clusters on a substrate (top view), (**d**) ordered nanonparticles on a substrate, and (**e**) simplified side view of a high-density recording medium

properties [69]—but the electronic structure of these units is very different from that of true clusters (Section 3.1).

An important practical point is the packing fraction of the clusters, which is roughly proportional to the magnetization M. Figures of merit of magnetic materials depend on M, as exemplified by the energy product of permanent magnets, which is quadratic in M. The packing also affects the hysteresis, especially via the demagnetizing factor [70]. Magnetic recording requires high-areal densities [29], but interactions between particles lead to harmful cooperative effects [4]. However, while we consider interactions, a detailed discussion of packing and compression issues goes beyond the scope of this chapter.

3.2.1 Synthesis of Supported Nanostructures

All bottom-up strategies for the fabrication of metallic nanostructures at surfaces are essentially based on growth phenomena. Atoms or molecules are deposited on the substrate in vacuum and nanoscale structures evolve as the result of a multitude of atomistic processes. Key processes during *epitaxial growth* are the surface diffusion of single adatoms, including diffusion on terraces, over steps, along edges, and across corners. Each diffusion step is thermally activated, with the respective rate depending exponentially on corresponding potential energy barrier. The shape and size of nanostructures are largely determined by the competition of active diffusion processes, and the growth temperature is the key for shaping the growing aggregates. The control over the epitaxial growth can be further increased by exploiting structured surfaces, such as stepped, reconstructed, or corrugated surfaces, as nanotemplates. Such surfaces offer predefined nucleation sites and the position of

each nanostructure is hence exactly defined by the template with nanometer accuracy (recent overview in [65]). However, surface free energies, lattice mismatch, or structural imperfections set limits to the epitaxial growth and most of the growth strategies work only for a few model systems.

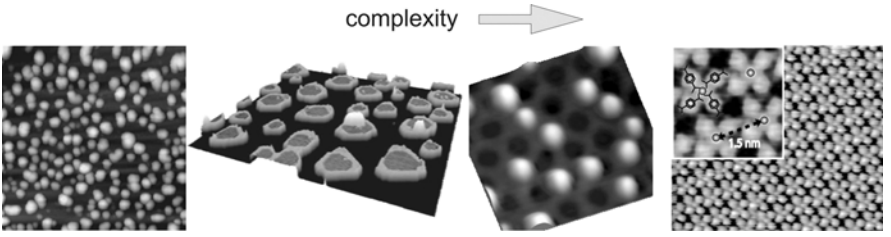

Fig. 3.3 STM images of surface-supported nanostructures of increasing complexity. From left: Fe clusters on Pt [71]; 2D core–shell particles of Fe cores (*grey*) with Pt shell (*bright*) on Pt substrate (*dark*) [72]; Co clusters, deposited on corrugated boron nitride template surface [73]; and Mononuclear $Fe(TPA)_4$ clover-leaf compounds from Fe-directed assembly of terephthalate organized in regular superlattices on Cu(100) [74, 75]

The complications associated with epitaxy can be overcome with *cluster deposition* methods, to fabricate cluster layers or cluster-assembled nanocomposites [64]. Here, the clusters are formed *before* they make contact with the surface. Mainly two techniques are established, which are soft-landing of clusters formed in the gas phase [76] and buffer-layer-assisted cluster growth (BLAG) [77–79]. Both techniques are, in principle, suitable to form clusters of almost any material on any substrate [80]. Advantages of BLAG are that (i) no experimental equipment beyond the standard molecular-beam epitaxy tools are required, (ii) it can be used to deposit clusters on nanotemplate surfaces, such as stepped substrates [81] or corrugated boron nitride monolayers ([82] and Fig. 3.3), to achieve controlled, ordered cluster arrangements, and (iii) the cluster formation is a parallel process and high cluster coverage can be achieved during a short preparation step. In contrast, the flux of dedicated cluster sources is limited by the mass filtering, but they usually give clusters with much narrower size distribution. Recent overviews over fabrication and properties of surface-supported clusters can be found in Refs. [83, 84]. A direct comparison between deposited and epitaxial Fe clusters illustrates best the effect of direct overlayer-substrate interaction during preparation and can be found, for instance, in Ref. [85].

Buffer-layer-assisted cluster fabrication requires pre-coating the substrate by a noble gas layer, such as Xe, at low temperature. Metal deposited on this buffer layer is mobile enough already at such low temperatures to form small clusters [79]. Warming up the substrate to 90 K causes evaporation of the Xe layer. The clusters coalesce during the Xe sublimation and thus grow in size, until making contact with the surface. The final cluster size and the size distribution depend mainly on the initial thickness of the Xe layer and on the metal coverage. Still on the Xe layer the cluster structure can partly relax. Figure 3.4 indicates that the site occupancy depends on size of the embedded particles. The corresponding statistical mechanics

is nontrivial and similar to the description of Krypton on graphite by the $q = 3$ Potts model [86]. We will return to these methods in the context of Fe–Pt thin-film nanostructures (Section 3.2.2).

Molecular self-assembly on metal surfaces is a powerful means to realize structurally complex nanosystems [55, 66, 87, 88]. Molecular networks are formed during the deposition of specific organic molecules on single crystalline metal surfaces under ultrahigh vacuum. Desired architectures can be obtained by controlling non-covalent interactions, such as hydrogen bonding, ionic bonding, and metal–ligand interactions, with the functional groups of the molecules. A particular class of network structures, the so-called metal–organic coordination systems (see Fig.3.3, right), is obtained by the co-deposition of functionalized organic molecules and metal atoms. The self-assembly depends here on coordination bondings between the two species. Metal–organic systems represent a fascinating form of magnetic material, as they are a lattice of metal centers with the lattice spacings defined by the molecules and interactions mediated by molecules and the surface. The symmetry of the networks can be controlled in a wide range by the design of the molecules and the preparation conditions [89–93].

3.2.2 Case Study: Fe Clusters on Pt Surfaces

The clusters of Fe, shown in the STM images in Fig. 3.4, have been produced by buffer-layer-assisted growth on pristine metal surfaces [71]. The cluster size and areal density are controlled during BLAG mainly by two parameters, namely by the thickness of the Xe buffer layer and by the coverage of the cluster material. The smallest clusters in Fig. 3.4, of less than 2 nm diameter, can be formed with 0.05 monolayers (ML) Fe and 2 ML Xe (a). For the images (b–d), 2 ML Fe and buffer layers of varied thickness between 5 and 45 ML have been used. We see that higher Xe layer thicknesses or higher Fe coverages result in larger clusters. The cluster density can also be controlled via both the Fe and the Xe coverage, and higher cluster densities are achieved with thin Xe layers and comparatively large Fe coverage (Fig. 3.4b). The diameter of the clusters of flattened hemispherical shape increases from 2.0 ± 1.0 to 9.9 ± 7.6 nm, from (a) to (d). Since STM tends to

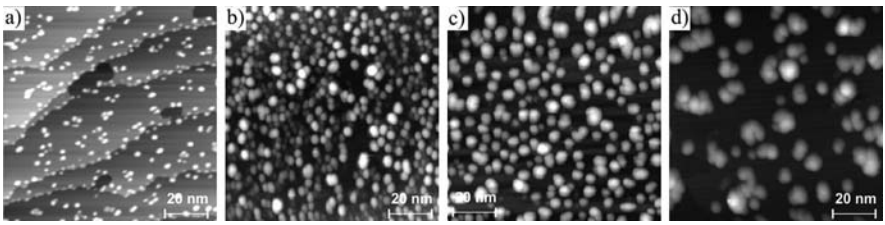

Fig. 3.4 Scanning tunneling microscopy (STM) pictures of Fe clusters fabricated by buffer-layer-assisted growth. (**a**) 0.05 ML Fe on Ag(111) using 2 ML Xe, (**b–d**) 2 ML Fe on Pt(997) using Xe buffer layers of 5, 18, and 45 ML thickness

overestimate the cluster size due to well-known tip convolution effects, the quoted cluster sizes are an upper limit. Without the Xe layer, the Fe is found to grow in the Volmer–Weber mode at substrate temperatures of 300 K and below [85]. Rough Fe films are obtained in this case with an average island size depending on the nominal Fe coverage.

Fe and Pt are known to form structurally and magnetically interesting phases in the bulk, such as Fe_3Pt (cubic Cu_3Au structure) and FePt (tetragonal $L1_0$ structure). The latter has a rather high magnetic anisotropy of about $5\,MJ/m^3$, which makes it suitable for ultrahigh-density magnetic recording [3, 94]. $L1_0$-ordered FePt can also be produced in thin-film form, although stacking sequences different from the original ABAB stacking yield modified electronic properties. However, supported growth offers completely new possibilities to form also other Fe–Pt structures of different stoichiometry, geometry, and coordination. Fe–Pt sub-nanostructures can been realized, for instance, on flat Pt(111) or the vicinal Pt(997) Pt surfaces, by exploiting simple rules of epitaxial growth [65]. By controlling only the growth temperature and the Fe coverage, low-coordinated atoms, dots, and wires of Fe on the Pt, as well as ordered or disordered FePt surface alloys can be formed (Fig. 3.5) [95]. The local atomic environment in all these structures is different from bulk alloys. The iron partially spin polarizes the Pt, which then exhibits spin, orbital moment, and magnetic anisotropy and contributes to, if not dictates, the magnetism of the Fe [96, 97].

In a thermodynamic sense, zero- and one-dimensional structures (dots and long wires) do not exhibit long-range ferromagnetic order but are *paramagnetic*. However, the interaction between wires and dots, realized by the Pt atoms, can make the system ferromagnetic. A very simple example is one fcc(111) monolayer of Fe atoms where every second monatomic row is replaced by Pt atoms, similar to the surface alloy in the right part of Fig. 3.5. Denoting the respective Fe–Fe and Fe–Pt exchange interactions by J and $J^* \ll J$ yields the mean-field Curie temperature

$$T_c = 2(J + J^{*2}/J)/k_B \tag{3.1}$$

It can be shown that the corrections to the mean-field approximation are comparable to the mean-field result itself [99], which makes even the simplest surface alloys quite intriguing.

A nontrivial question is the onset of ferromagnetism in low-dimensional systems. It can be shown exactly that one-dimensional 'ferromagnets' are actually paramagnetic [100–102]. The proof for thin-film stripes of width w and thickness t is similar to the argumentation for the Ising model [100], except that the Ising bonds J must be replaced by effective exchange bonds scaling as $J_{\text{eff}} = 4tw(AK_{\text{eff}})^{1/2}$, where A and K_{eff} are the exchange stiffness and effective anisotropy, respectively [3] of the film. Kinetic barriers to reaching equilibrium, as considered in [67], are irrelevant to the problem, because ferromagnetism is defined as an equilibrium property. A slow approach toward equilibrium may mimic ferromagnetic order. The kinetics merely decides how long it takes to establish equilibrium [102] and structures larger than 1 or 2 nm behave bulk like.

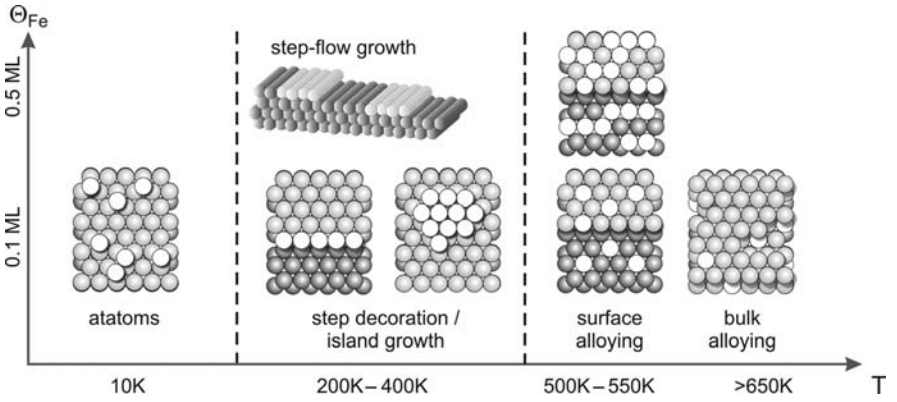

Fig. 3.5 Top-view on magnetic Fe–Pt surface structures (schematic). The brightest colors represent Fe atoms and darker colors represent Pt atoms in different layers. A variety of different Fe–Pt nanostructures can be fabricated by controlling only the substrate temperature during Fe deposition (T) and the Fe coverage (θ_{Fe}). The increased mobility at higher temperatures promotes chain or stripe formation on Pt(997) or compact cluster formation on Pt(111), and eventually surface and bulk alloying [98]

3.2.3 Structure of Embedded Clusters

Let us now discuss the structure and properties of clusters that are embedded in a matrix. Such cluster systems, for example Fe-Pt, Co-O, Mn-Au and Ti-O, can be produced by cluster deposition (Sect. 3.2.1) and other methods. The formation of clusters in a solid matrix can often be considered as an addition of substitutional or interstitial atoms. Figure 3.6 shows that here is a major distinction between coherently embedded and precipitated clusters. In dilute magnetic oxides and other systems, there may be segregated phases with distinct lattice parameters and structures (d), or coherent clustering with some lattice strain but without topological disruption of the lattice (c). This phenomenon applies to both substitutional and interstitial atoms and has many parallels in other areas of magnetism (C in Fe, N in $Sm_2Fe_{17}N_3$). It is related to *spinodal decomposition* and involves phenomena such as negative diffusion constants (see below). In many cases, the site occupancy is random (not shown in Fig. 3.6), and there is a general trend toward randomness above a structural ordering temperature T_c. The mean-field description of this transition is known as the Gorsky–Bragg–Williams model and predicts that T_c is proportional to the interatomic interaction strength.

The model is actually very similar to the spin-1/2 Ising mean-field model, except that the average spin variables $s_i = \pm 1$ (or $\uparrow$ and $\downarrow$) are replaced by the concentration $c_i = 0$ (A-atom) and $c_i = 1$ (B-atom). The relation between c_i and s_i is therefore $c_i = (1 + s_i)/2$, and the mean-field equation

$$< s >= \tanh\left(\frac{zJ < s > +h}{k_B T}\right) \tag{3.2a}$$

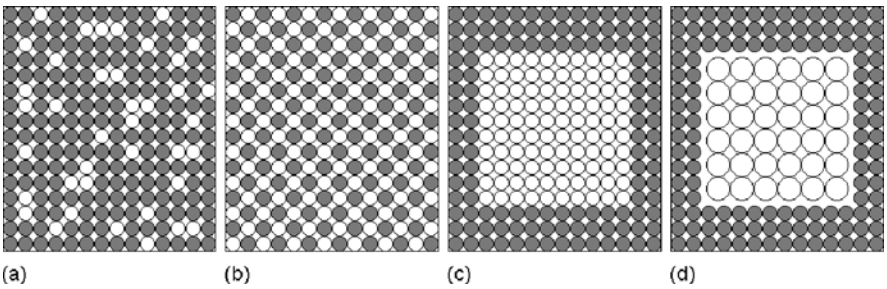

Fig. 3.6 Embedding of atoms in a matrix: (**a**) solid solution, (**b**) alloy, (**c**) coherent embedding, and (**d**) incoherent embedding or precipitation. These mechanisms are realized in a variety of nanostructures, including dilute magnetic semiconductors

becomes

$$< c >= \frac{1}{1 + \exp\left(\dfrac{4zJ < c > +h - 2zJ}{k_{\mathrm{B}}T}\right)} \tag{3.2b}$$

In the latter equation, J is a (non-magnetic) net interaction energy between A and B atoms. The external field (or force) variable h has the character of a chemical potential and fixes the total numbers of A and B atoms [103]. In both cases, z is the number of nearest neighbors ($z = 4$ in the simplified model of Fig. 3.6b), and the mean-field ordering temperature $T_{\mathrm{c}} = z|J|/k_{\mathrm{B}}$. Above T_{c}, the structures of (b) and (c) are destroyed.

Treating the dynamics of the structures on a mean-field level amounts to the introduction of an effective diffusion constant [105, 206],

$$D = D_{\mathrm{o}}\left(1 - 4c(1-c)\frac{T_{\mathrm{c}}}{T}\right) \tag{3.3}$$

where D_{o} is the interaction-free diffusivity and $\mathrm{c} = <\mathrm{c}>$ is the concentration of the impurity atoms. An important special case is spinodal decomposition, that is, the transition from Fig. 3.6a to c.

A striking feature of (3.3) is the prediction of negative diffusion constants D. Ordinary diffusion means that initial concentration gradients are smoothed, whereas negative diffusion constants lead to the enhancement of pre-existing concentration inhomogenities. Figure 3.7 illustrates this point by showing the evolution of a concentration inhomogenity for $D < 0$, eventually leading to phase segregation, Fig. 3.6c. Interestingly, there are three cases where the diffusivity is concentration independent. First, for small concentrations ($\mathrm{c} \sim 0$), we obtain the trivial limit $D = D_{\mathrm{o}}$, roughly corresponding to Fig. 3.6a. Second, for high concentrations ($\mathrm{c} \sim 1$), one obtains $D = D_{\mathrm{o}}$, meaning that dense systems behave like diluted systems. This is a diffusion analogy to dense electron gases, which behave like non-interacting

particles. The underlying physics is the division of the phase space into cells, namely crystal sites in diffusive systems and k-space cells in electron gases. Then, the hard-core repulsion of the atoms and the Pauli principle, respectively, reduce the importance of interactions. Alternatively, one may consider diffusing holes rather than diffusing particles. The third exception is the limit of high temperatures: since $c(1-c) \leq 1/4$, negative diffusion coefficients are limited to $T \leq T_c$ and $D = D_o$ for $T = \infty$.

The role of attractive interactions between A (or B) atoms is seen from the ideal-gas analogy. A non-interacting hard-core gas can be compressed to a relatively dense random packing fraction of about 64%, but it never becomes a fluid with different high and low-density phases. The interactions between diffusing atoms are largely elastic [103, 104]. The electronic interactions determine the solubility, parameterized by h in (1b), and ensure the hard-core repulsion between atoms, but their contribution to J is negligible. Due to the size difference between A and B atoms, Fig. 3.6c is elastically more favorable than Fig. 3.6c, so that spinodal decomposition is a very common phenomenon, especially for interstitial impurities. However, some alloys have strong A–B interactions, and the resulting structure is similar to Fig. 3.6b. Examples are $L1_0$ alloys, such as FePt, where the light and heavy transition-metal atoms form layers, and the surface alloys discussed in the following subsection.

An interesting point is that the mean-field approximation works well for impurity atoms if the summation $zJ = \Sigma_j J_{ij}$ includes more distant atoms. This is different from the magnetic Ising model, where the critical exponents become incorrect in fewer than four dimensions [104, 105]. Note that the elastic energy of Fig. 3.6c is smaller than that of (a), but a global minimum of the elastic energy is achieved by incoherent phase segregation, Fig. 3.6d. For large atomic-size differences, the incoherent state is the only one that can be realized in practice. Experimentally, (d) yields two well-separated x-ray diffraction peaks, but (a–c) are more difficult to distinguish.

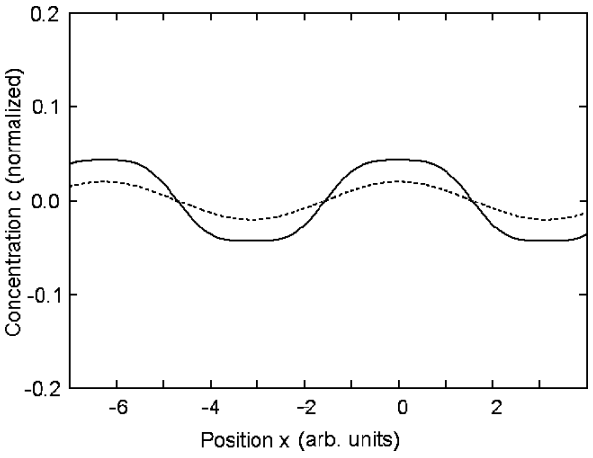

Fig. 3.7 Effect of negative diffusion constants during spinodal decomposition. In contrast to ordinary diffusion, initial concentration gradients (*dotted line*) are enhanced during the diffusion (*solid line*)

3.2.4 Case Study: FePt Clusters in a Carbon Matrix

Recently, interest in films based on magnetic nanoclusters has grown enormously with increasing attention devoted to the extension of the magnetic recording areal density to 1 terabit/in^2 and beyond. This depends on the development of high-anisotropy films with uniform size clusters or grains below 10 nm that are exchange decoupled or weakly coupled [29, 106, 107]. The Equiatomic FePt nanoclusters with $L1_0$ phase are a promising candidate for such media, because of their large anisotropy constant K of about $\sim 7 \times 10^7$ erg/cm [107, 108], which helps to meet the requirement for both high signal-to-noise ratio and thermal stability of the media.

While many efforts have been made to fabricate oriented $L1_0$ FePt nanoparticle or nanograin films with some exchange coupling [109, 110], understanding the magnetic properties of a collection of well-isolated clusters is of similar high interest for exploring FePt clusters as a potential media for extremely high-density recording. Xu et al. [111] have prepared FePt nanoclusters with small average cluster size ($d \sim 4$ nm) using a gas-aggregation technique [112]. The FePt clusters are nearly monodispersed with a narrow Gaussian size distribution (standard deviation $\sigma / d \sim 0.09$). Dilute FePt:C nanocluster films have been prepared, in which the FePt volume fraction ranged from 5 to 30%. Carbon was used as the matrix for isolating the FePt clusters to decrease the exchange interaction and to reduce the cluster growth during high-temperature annealing.

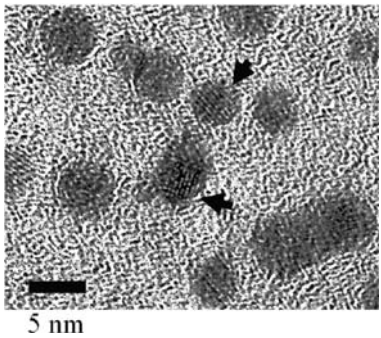

Fig. 3.8 TEM image of FePt:C cluster film with 5 vol% FePt annealed at 700°C for 10 min

Figure 3.8 shows a TEM image of FePt:C cluster film with 5 vol% FePt annealed at 700°C for 10 min. Well-isolated clusters with single crystal $L1_0$ structure are observed. The arrows indicate the clusters with lattice fringe observable, suggesting single crystalline clusters.

Figure 3.9a shows the in-plane and perpendicular hysteresis loops of the FePt:C film with 5 vol% FePt annealed at 700°C for 60 min, measured at 10 K. Both in-plane and perpendicular loops are similar, indicating that the easy axes of the FePt clusters are distributed randomly, which is in agreement with the XRD measurement. A perpendicular coercivity of about 29 kOe at room temperature and 40 kOe at 10 K are achieved. This result indicates the high degree of $L1_0$ ordering after annealing for a relatively long time (> 10 min). The loops are not saturated at an applied

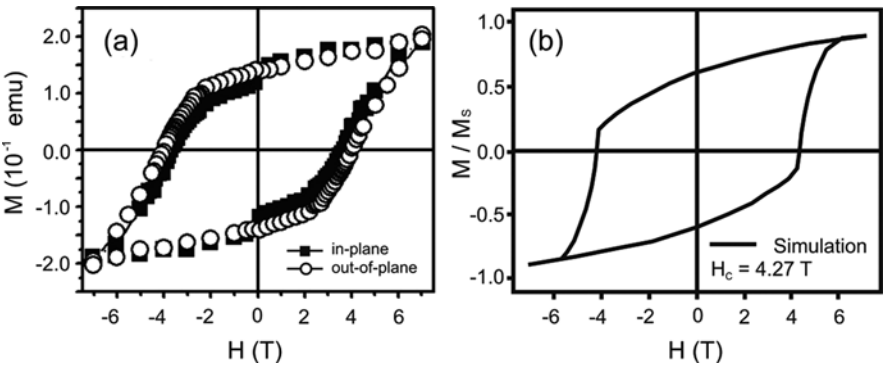

Fig. 3.9 In-plane and perpendicular hysteresis loops of FePt:C cluster films with 5 vol% FePt annealed at 700°C for 60 min: (**a**) at 10 K; (**b**) hysteresis loop obtained by numerical simulation based on Landau–Lifshitz–Gilbert equation

field of 70 kOe. Assuming these isolated clusters are non-interacting and the formula $H_c = 0.48\ H_k$ can be applied [113], an anisotropy field $H_k = 2K/\mu_o M_s$ of 8.3 T [83 kOe] is obtained. This estimate is confirmed by a numerical simulation using the NIST OOMMF code based on Landau–Lifshitz–Gilbert equation.[1] The simulation assumes $L1_0$ FePt spheres of diameter of 4.5 nm. The spheres occupy 5% of the total volume and are randomly oriented in a non-magnetic matrix, without intergranular exchange interactions. The chosen parameters are the anisotropy constant $K = 4\ \mathrm{MJ/m^3}$ and the saturation magnetization $M_s = 1.13$ T [900 emu/cm^3], corresponding to $H_k = 8.9$ T, as well the exchange stiffness $A = 10$ pJ/m. The simulated hysteresis loop, Fig. 3.9b, is essentially a Stoner–Wohlfarth loop for randomly oriented particles, and its coercivity of 4.27 T is close to the experimental value of 4 T at 10 K. This confirms that the 5 vol% of FePt clusters in the C matrix behave like non-interacting Stoner–Wohlfarth particles. Such a system may show useful and more interesting nanomagnetism if the orientation of the clusters can be controlled, which needs to be further investigated.

3.3 Anisotropy and Hysteresis

The control of anisotropy and hysteresis is one of the key aims of magnetic nanostructuring. Anisotropy means that the magnetic energy depends on the angle between magnetization and crystal (or nanostructure) axes. In contrast, interatomic exchange refers to the *relative* orientation of neighboring atomic spins. Magnetic hysteresis and coercivity reflect energy barriers caused by magnetic anisotropy, although the barriers depend on the exchange, too. Both anisotropy and hysteresis are real-structure dependent. The real-structure dependence of the anisotropy is

[1] http://math.nist.gov/oommf/

epitomized by surface and interface anisotropies, whereas hysteresis and coercivity are often affected by seemingly small imperfections. For example, tiny additions of N or C may enhance the coercivity of pure iron by several orders of magnitude [69, 114].

The practical importance of anisotropy and coercivity cannot be overestimated. In soft magnets, low coercivity is desired and achieved by embedding of Fe–Si nanoparticles of random-anisotropy in a three-dimensional matrix [115, 116]. Permanent magnets are usually characterized by high anisotropies and coercivities, whereas ultrahigh-density recording media combine well-defined hysteresis loops with sufficient anisotropy and reasonably low writing fields. The focus of this section is on some aspects of the anisotropy of *embedded* nanostructures. There is a rich literature on specific magnetization-reversal mechanisms [3, 58, 117–121] and the resulting hysteresis loops in various systems, such as soft magnets [116], permanent magnets [23, 69, 122–124], and recording media [47, 49].

A long-standing challenge in nanomagnetism is the thermal stability of the magnetization direction. For a small particle of volume V and anisotropy K, the relaxation time

$$\tau = \tau_o \exp(KV/k_B T) \tag{3.4}$$

where $\tau_o \sim 10^{-10}$ s. The particle volume is usually limited, so that room temperature thermal stability requires the control and enhancement of the anisotropy, including surface and interface anisotropy contributions. Thermally stable hard-magnetic Fe–Pt nanoparticles can now be produced down to 3 nm [22], and much work is presently being done to understand and exploit the lower end of these length scales, especially in ultrahigh-density magnetic recording. Based on present-day bulk materials ($SmCo_5$), stable room temperature ferromagnetism is possible down to particle sizes of slightly less than 2 nm. $SmCo_5$ is quite corrosive and therefore not suitable as traditional recording material. However, future recording may be realized by sealed drives, partially for tribiological reasons, which could put $SmCo_5$ in the spotlight again.

3.3.1 Surface and Interface Anisotropies

Magnetostatic contributions, such as shape anisotropy, are important in some materials. However, the leading anisotropy contribution is usually magnetocrystalline and reflects the interplay between crystal–field interaction (including hopping) and spin–orbit interaction. This includes not only bulk anisotropies but also surface, interface, and magneto-elastic anisotropies. The magnetic surface anisotropy adds to the total anisotropy [3, 125, 126].

In a nutshell, magnetocrystalline anisotropy reflects aspherical current loops (orbital moments) created by the spin–orbit coupling. These orbital-moment electron clouds interact with the atomic environment (crystal field), resulting in a directional dependence of their orientation which is observed as magnetocrystalline

anisotropy. It is important to keep in mind that symmetry breaking at surfaces and interfaces is a necessary but not sufficient condition for magnetic anisotropy. For example, the Heisenberg model (Section 3.1) is intrinsically *isotropic*, that is, the exchange energy does not depend on the angle between magnetization direction and bond axis $\mathbf{r}_i - \mathbf{r}_j$. A challenge is that surface anisotropy is closely linked to the *indexing* of the surface [3, 121, 133], which makes the frequently assumed normal anisotropy $-K\,(\mathbf{s}\cdot\mathbf{n})^2$ [126, 205] a very crude approximation.

The calculation of the anisotropy is often complicated [127, 128], but there exist simple models for a variety of limiting cases [69, 120, 129, 130]. For example, rare-earth anisotropy is characterized by a spin–orbit coupling much larger then the crystal–field interaction. This leads to a rigid Hund′s-rules coupling between spin and orbital moments and means that the anisotropy energy is essentially equal to the electrostatic interaction energy between the rare-earth 4f shells and the crystal field [69, 120]. Most rare-earth shells are aspherical and yield large anisotropy contributions, but gadolinium (Gd) has a half-filled 4f shell ($4f^7$) with spherical symmetry and zero magnetocrystalline anisotropy.

The crystal–field character of the anisotropy is seen, for example, from the possibility of changing the magnetization direction of Ni due to reversible absorption of H on Ni/Cu(001) [131]. A similar mechanism, namely the interstitial absorption of N, can be used to turn the soft magnetic material Sm_2Fe_{17} into hard-magnetic $Sm_2Fe_{17}N_3$ [105]. In itinerant 3d metals, the electron density $\psi^*(\mathbf{r})\psi(\mathbf{r})$ is largely determined by the interatomic hopping (band structure), and the spin–orbit coupling is a small perturbation [132]. The relation between crystal–field (hopping) and anisotropy can no longer be mapped onto a simple electrostatic interactions [120, 129, 133], but it remains possible to postulate rules for limiting cases, such as nearly filled 3d shells (Section 4.3)

An unusual surface magnetic anisotropy occurs in MnO nanoparticles. Mn^{2+} has a half-filled shell (3d5) and should be isotropic in any environment, similar to the role of Gd in the rare-earth series. The anisotropy of bulk MnO is indeed very small, but there is a striking anisotropy enhancement in nanoparticles [134]. This is explained in terms of a high-spin–low-spin transition created by the strong crystal–field interaction at the surface. The crystal field causes majority 3d electrons to jump to low-lying minority states and creates anisotropy in the Mn atoms [134].

3.3.2 Hysteresis of Fe Clusters on Pt

Let us now return to the Fe/Pt system introduced in Section 3.2.2. Figure 3.10 shows Kerr-effect (MOKE) hysteresis loops for an epitaxially grown Fe layer of nominally deposited 2 ML of Fe (left), and cluster ensembles formed from the same amount of Fe on Xe layers of the indicated thickness (see STM images in Fig. 3.4). For the clusters, preferential in-plane magnetization is found, in contrast to the perpendicular anisotropy found for the epitaxial Fe layer. The increase of the average cluster size with Xe buffer layer thickness enhances the total magnetic signal. Due to a

distribution of the cluster size and orientation, the loops are not saturated at the maximum available field.

For all samples shown in Fig. 3.4, the magnetic anisotropy is significantly enhanced with respect to bulk Fe [71]. This is the result of the large Fe–Pt interface anisotropy caused by the hybridization of iron-series 3d and heavy transition metal 4d/5d electrons (Section 3.3.3). By choosing suitable combinations of substrate and clusters, it is possible to tune the magnetic anisotropy of the clusters, and values of up to 0.9 meV/atom and 9 meV/atom have been reported for smallest Fe and Co clusters on Pt [135]. In addition, STM images reveal the presence of significant strain in epitaxial Fe islands on Pt(117) due to the lattice mismatch. The corresponding magneto-elastic contribution to the anisotropy energy is sufficient to overcome the shape anisotropy, thus favoring perpendicular magnetization [85].

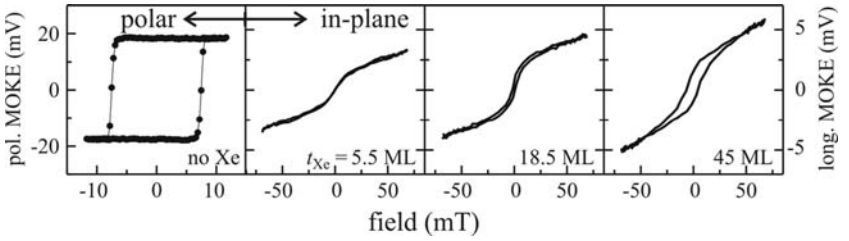

Fig. 3.10 MOKE hysteresis loops of 2 ML Fe on Pt(997) prepared on Xe buffer layers of varying thickness between 0 and 45 ML. Without Xe, Fe grows epitaxially in Vollmer–Weber mode [68], while the Xe layer promotes the formation of partially relaxed Fe clusters. The cluster size increases with the Xe thickness, see Fig. 3.4

The evaluation of experimental hysteresis loops and the determination of the anisotropy are complicated by the unknown moment of the clusters. In fact, the surface enhancement of the magnetic moment in clusters can even exceed the moments found in monolayer thin film or in metallic surfaces [136]. Ignoring interactions, the deposited particles are superparamagnetic, and their anisotropies can be estimated form the superparamagnetic blocking temperature T_B, which can be determined experimentally from temperature-dependent MOKE measurements (Fig. 3.11). Taking the average cluster volume from STM images and putting $\tau \sim 100$ s in (3.4) gives an estimate for the anisotropy of the clusters, which is $K = 13\,\mu$eV per atom for clusters of 2 ML Fe and 45 ML Xe (compare to bulk Fe: 4 μeV per atom). The anisotropy energy per atom in the cluster might actually be larger since STM tends to overestimate the cluster volume. The importance of finite-temperature effects is also seen from Fig. 3.11; the pronounced decrease of magnetization and coercivity is a consequence of Eq. (3.4).

The net magnetization of clusters can be stabilized by inter-particle and particle–substrate interactions [37, 38, 137, 138]. In the present case, the dominant contribution to the magnetic anisotropy is expected to come from the interaction of the clusters with the substrate. The clusters hybridize with the underlying substrate, thus producing a cloud of magnetic polarization in the Pt [139, 140]. Although the

contact to the substrate somewhat reduces the average spin moment per atom in the cluster, it introduces a moment in the d-band of the substrate, which might even be extended beyond the region of physical contact [141]. Hence, the effective magnetic volume as well as the anisotropy is increased, which stabilizes the overall magnetization, increases the blocking temperature, and ties the cluster magnetization to the substrate lattice. However, this leads to cooperative magnetization reversal [3] and goes at the expense of the effective cluster size, eventually reducing the areal density in magnetic recording. Furthermore, (3.4) is limited to very *small* particles [59]. In large particles, incoherent magnetization processes and thermal excitations reduce the volume V to some effective volumes $V_{\text{eff}} < V$. For example, magnetization reversal in long and highly anisotropic wires requires a thermal energy of $4\pi R^2(AK)^{1/2}$, corresponding to $V_{\text{eff}} = 4\delta_B R^2$, where R is the wire radius and $\delta_B = \pi(A/K)^{1/2}$ is the Bloch-wall width of the wire. In other words, making wires very long yields large values of KV but no proportional increase in thermal stability.

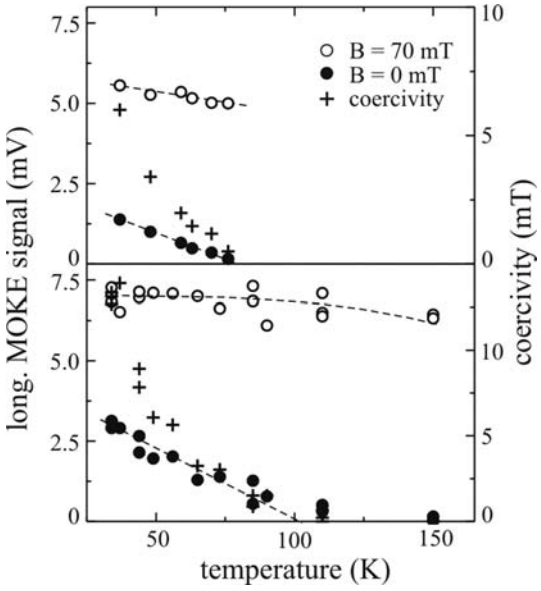

Fig. 3.11 Temperature dependence of the coercivity (+), the longitudinal MOKE signal at remanence (•), and in a field of 70 mT (o) for 2 ML Fe/45 ML Xe/Pt(997) (*top*) and 4 ML Fe/18 ML Xe/Pt(997) (*bottom*). The blocking temperature increases with the cluster size. The MOKE measurements have been done after Xe desorption at 100 K

3.3.3 Role of Heavy Transition Metals

The spin polarization of exchange-enhanced Pauli paramagnets in compound structures affects not only the magnetic moment but also the anisotropy. This is because the 4d and 5d elements are much heavier than the 3d elements and exhibit a more pronounced spin–orbit coupling. This explains the pronounced anisotropy of $L1_0$-ordered 3d/4d and 3d/5d magnets, such as the FePt, CoPt, and FePd [94], as well as the ′giant′ [135] anisotropy of various thin-film structures. Since a single late 3d

atom can spin polarize several 4d or 5d atoms, the anisotropies per 3d atom can actually be huge, for example, 9 meV for one Co atom on Pt(111) [135]. In thin-film nanostructures, such as those shown in Fig. 3.3 or Fig. 3.5, the effect strongly depends on the chemical nature and indexing of the substrate, on the structure and shape of the clusters, on the lattice mismatch (strain), and on the reduced coordination.

However, the main contribution to the anisotropy comes from the heavy transition metals, and the anisotropy per Pt atom is relatively large but not surprising. In fact, even larger values can be achieved in 5f compounds, but as in the Co/Pt(111) system, these high values are limited to low temperatures [130]. Incidentally, the temperature dependence of these structures is quite intriguing, with substantial deviations from the popular Callen-and-Callen theory [142–144].

The spin polarization also affects the *dynamics* of thin-film structures, because spin–orbit coupling is a major source of damping. The effect is also known as spin pumping [145], although it is somewhat different from the spin pumping usually considered in magneto-transport. Figure 3.12 shows a typical geometry. As in other inhomogeneous nanostructures [146–148], the magnetization modes are localized, and the damping comes from the regions where both the magnetization and the spin–orbit coupling (λ) are large. Physically, iron-series 3d electrons hop onto Pt sites, where they give rise to damping via the spin–orbit interaction of the Pt 5d electrons. Since the Co ensures a significant spin polarization in the Pt, the effect is large in Fig. 3.12a. In (b), the Ni is essentially unable to spin polarize the Pt and may actually become paramagnetic at the interface. This means that the damping is larger in the Co/Pt systems than in the Ni/Pt system. The effect can be investigated experimentally, by using optical pump-probe techniques [209] or FMR [145].

An idea related to the magnetic anisotropy of 3d/4d and 3d/5d thin-film nanostructures is the exploitation of heavy transition metals such as W in permanent magnetism and ultrahigh-density magnetic recording. One example is the Fe–W system [149]. In fact, there are many ferro- and antiferromagnetic $L1_0$-type compounds [96, 150–154], and many alloys exhibit easy-axis anisotropy along the *c*-axis, especially those containing Pt and Pd, whereas MnRh has in-plane anisotropy [96]. This reflects the orientation of the easy axis to the bond axis of itinerant magnets [129].

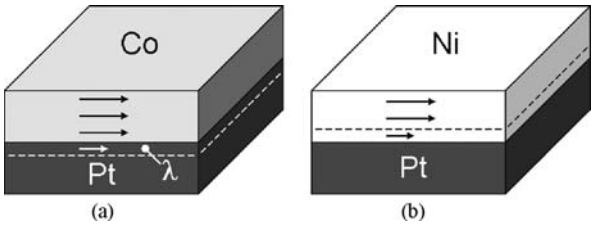

Fig. 3.12 Damping at Co–Pt and Ni–Pt interfaces. The damping is much larger in Co–Pt, because the Co yields a substantial spin polarization in adjacent Pt atoms, which then realize damping via the strong spin–orbit coupling (λ) of the Pt 5d electrons

Aside from binary $L1_0$ compounds, one can consider alloys with the general composition $A_xB_yC_z$, where A = Fe, Co, B = Pd, Pt, C = Mn, Ni, Cu, W, Rh, Ir, and x, y, and z are compatible with the stoichiometry and solid-solution range [152–154] of the tetragonal $L1_0$ phase. Similar considerations apply to materials crystallizing in the hexagonal NiAs structure, especially MnBi and PtBi. Based on these materials, two-phase nanostructuring can be used to tailor the magnetic anisotropy. Anisotropy is an atomic quantity, but the ferromagnetic exchange ensures an anisotropy averaging over a few nanometers, in contrast to the absence of nanoscale Curie temperature averaging [120, 155]. In particular, the intriguing temperature dependence of the anisotropy of many alloys [130, 144] opens the door for the creation of temperature-dependent anisotropy zeros, with a useful write-field reduction in magnetic recording. On an atomic scale, a similar effect is well known to occur in alloys such as Fe–Co–Tb–Dy but limited to a relatively narrow range of rare-earth transition-metal intermetallics [156]. Nanostructuring offers a way to greatly extend the range of these materials.

3.3.4 Proteresis

Nanoscale embedding may yield properties and phenomena not encountered in bulk magnets and single-phase nanostructures. One example is the occurance of inverted hysteresis loops (or proteresis) in CoO/Co core–shell nanostructures. The effect was originally discovered in granular nanocomposites and means that the hysteresis loop is cycled clockwise rather than anticlockwise [157]. The phenomenon is counterintuitive, because it means that magnetostatic energy is created rather than dissipated. The basic explanation [157] involves an energy transfer between magnetic and exchange energies, so that the net energy is well behaved.

Proteresis has recently been observed in ultrasmall Co:CoO core–shell nanoclusters [8]. The structures, produced by cluster-beam deposition, have Co core sizes ranging from 1 to 7 nm and a common CoO shell thickness of about 3 nm. Figure 3.13 shows that the proteretic behavior reflects a subtle interplay between various anisotropies and exchange interactions in the Co and CoO phases and at the Co–CoO interface. A striking feature is the existence of proteretic (clockwise) rather than hysteretic loops in a relatively narrow core size range from 3 to 4 nm—smaller and larger particles exhibit ordinary hysteresis loops.

The size dependence is explained by first considering a very small soft-magnetic core in a hard matrix. The hard and soft regions are then strongly exchange-coupled, and the core–shell cluster rigidly rotates in a magnetic field, and the loop is hysteretic. In the opposite limit of large core–shell clusters, the system behaves like a superposition of two phases, both hysteretic. Only on a length scale of a few nanometers, where the interactions shown in Fig. 3.13b–c are comparable, proteresis is observed.

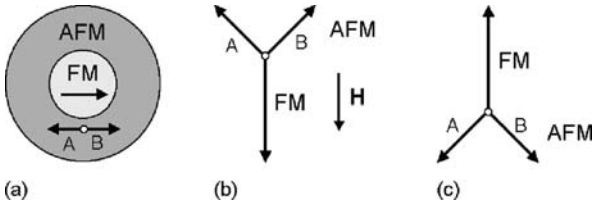

Fig. 3.13 Proteresis in Co:CoO core–shell nanoparticles: (**a**) structure and sublattice magnetizations, (**b**) initial spin structure and (**c**) final spin structure. In (**b**), the magnetic field acts on the sublattices *A* and *B* of the AFM CoO, but not on the FM magnetization of the core

3.4 Quantum-Mechanical Effects

Both free and embedded nanostructures exhibit interesting quantum effects [21, 158], although the relative importance of those effects tends to decrease with increasing feature size and is often difficult to distinguish from classical real-structure effects [159]. According to quantum mechanics, electrons behave like waves, and the embedding of an atom or cluster in a bigger unit tends to mix the wave functions both in the cluster and in the matrix. The range of those interaction is rarely much larger than 1 nm, but this is sufficient to create major changes.

A crude way of gauging of the effect of nanostructuring on the anisotropy is to compare the spin–orbit coupling λ (about 0.05 eV for the late 3d metals) with the 3d band width of about 5 eV. This means that minor structural changes may have a strong impact on the anisotropy, and depending on the individual energy levels near the Fermi level, the effect may extend over several nanometers. Anisotropy rules for itinerant ferromagnets are therefore more difficult to establish than for rare-earth magnets.

3.4.1 Embedding from a Quantum-Mechanical Point of View

How do the quantum states change when an isolated cluster is embedded in a matrix? A conceptually simple—though practically often demanding—procedure is the mapping of the complex states onto simpler wave functions, such as hybridized atomic states or extended orbitals. The corresponding procedure is known as *downfolding* [160–162] and goes back to a perturbation approach by Löwdin [163]. The idea is to divide the quantum states $|\psi>$ of the full system into arbitrary classes, which yields a relatively simple formula describing the interaction between subsystems. In solids, downfolding is used to simplify Hamiltonians and to introduce physically transparent extended orbitals (including third-nearest neighbors). This method was successfully applied, for example, to high-temperature superconductors [162].

In the present case, it is natural to choose the quantum states $|\phi>$ of the embedded cluster or nanostructure as the first class and the quantum states $|\chi>$ of the

embedding matrix as the second class. The Schrödinger equation $H|\psi> = E|\psi>$ can then be written as

$$H_{cluster}|\phi> + V|\chi> = E|\phi> \tag{3.5a}$$

and

$$V^{+}|\phi> + H_{matrix}|\chi> = E|\chi> \tag{3.5b}$$

where V describes the interaction between cluster and matrix. Substitution of $|\chi>$ into 3.5(a) yields

$$H_{cluster}|\phi> + V\frac{1}{E - H_{matrix}}V^{+}|\phi> = E|\phi> \tag{3.6}$$

This equation is the type $H_{eff}\ |\phi> = E\ |\phi>$, where H_{eff} is an effective interaction and may by solved by various methods. For example, one can first diagonalize H_{matrix} and label the eigenvalues by k, so that $1/(E - H_{matrix})$ becomes $1/(E - E_k)$. As a special case, (3.6) yields ordinary perturbation theory [163].

Equation (3.6) is remarkable, because it does not contain the unknown wave function $|\chi>$ of the matrix but yields the exact energy eigenvalues. The downside and practical challenge is the energy dependence $H_{eff}(E)$ of the effective Hamiltonian. Consider, for example, a single impurity level $|\phi>$ in a solid. If H_{eff} was independent of E, then the energy would be given by $E = <\phi|H_{cluster}\ |\phi> + <\phi|\ H_{eff}\ |\phi>$. However, for each eigenstate of $H_{cluster}$, the E in the denominator of (3.6) creates additional roots of the secular equation. The corrections are particularly large when the eigenvalues of the clusters (E) are comparable to those of the matrix (H_{matrix}). This is particularly common in metals, where the bulk states form rather broad bands and easily hybridize with the discrete states of the embedded objects if they have comparable energies.

3.4.2 Exchange Interactions

The Curie temperature and many other magnetic properties, such as the temperature dependence of the anisotropy, reflect interatomic exchange. On a one-electron level, exchange is obtained by making the potential spin dependent, as in the Stoner model and in LSDA calculations. On a many-electron level, there are correlation corrections, with the Heisenberg model as an extreme limit (Section 3.3). Here, we focus on a simplified model, namely on the Ruderman–Kittel–Kasuya–Yosida (or RKKY) model [164]. The idea is to model two spins S and S' at $\mathbf{r}$ and $\mathbf{r}'$, respectively, by a point-like interaction J with conduction electrons s_n. The effect of the S and S' can then be described perturbatively, by equating the conduction electron Hamiltonian with H_{matrix} in (3.6) and applying perturbation theory.

A key feature of the free-electron RKKY exchange [164] is its long-range oscillatory behavior, which is caused by the sharp Fermi surface and described by $J_{ij} = \sim \cos(2k_F r)/r^3$, where k_F is the Fermi wave vector and $r = |\mathbf{r}_i – \mathbf{r}_j|$ is the distance between the spins. The oscillations means that spatial features smaller than about $1/k_F$ cannot be resolved with the available zero-temperature wave functions. Interestingly, net RKKY interactions do not average to zero but actually *increase* when embedded atoms are replaced by embedded nanoparticles, although the size-dependent increase is less pronounced than of the magnetostatic energy [165].

While traditional RKKY theory considers conduction electrons, the same approach can be used to treat tightly bound electrons [166] and electron orbitals localized around impurities [167]. The latter is of interest for dilute magnetic semiconductors [168–174], where structures similar to Fig. 3.6a yield ferromagnetism at and above room temperature.

Let us assume that the exchange between the two localized 3d spins is mediated by s electron (or hole) states from shallow donors or acceptors, which hybridize and may or may not form a narrow band. The calculation of the exchange amounts to the evaluation of the total energy for parallel and antiparallel spin orientations $S_i = \pm S_j$. The corresponding energies are

$$E_{\pm} = \Sigma_{\mu} \frac{| < \Psi_{\mu} | V(S_i) \pm V(S_j) | \Psi_o > |^2}{E_{\mu} - E_o} \tag{3.7}$$

where $|\Psi_{\mu} >$ describes the mediating electrons and the interaction potential V is of the s–d type

$$V_i(\mathbf{r}) = \pm J_o S_i \delta(\mathbf{r} - \mathbf{r}_i) \tag{3.8}$$

Here, the sign indicates whether the mediating electron is ↑ or ↓. When both localized (3d) spins are located in one single-occupied shallow orbital, then the exchange is ferromagnetic, irrespective of the sign of J_o, because both 3d spins are parallel (or antiparallel) to the spin of the shallow electron. With increasing impurity concentration, the shallow orbitals overlap and eventually percolate. Since the shallow orbitals have a radius of the order of 1 nm, this happens at very low concentrations.

Consider the exchange mediated by two overlapping shallow orbitals located at $\mathbf{R}_1$ and $\mathbf{R}_2$. The hybridized wave functions have the character of (anti)bonding states whose level splitting is determined by the hopping integral t, and (3.7) yields the exchange [167]

$$J_{ij} = -\frac{J_o^2}{8t} \left(\rho\left(r_i - R_1\right) - \rho\left(r_i - R_2\right)\right) \left(\rho\left(r_j - R_1\right) - \rho\left(r_j - R_2\right)\right) \tag{3.9}$$

where r denotes the hydrogen-like density $\Psi^* \Psi$ of the shallow electrons. Here the involvement of ${J_o}^2$ reflects the second-order perturbation character of the theory, whereas the level splitting $E_{\mu} - E_o \sim t$ originates from the denominator in Eq. (3.2a,b).

Equation 3.9 is separable and can be interpreted in terms of Fig. 3.14: the exchange is ferromagnetic (FM) if the magnetic ions are located in the same shallow s-orbital (a) and antiferromagnetic (AFM) if they are in different s-orbitals (b). The dashed line in the figure provides an alternative explanation: spins on the same side of the line exhibit FM coupling, whereas spins separated by the dashed line exhibit AFM coupling.

In contrast to the free-electron RKKY exchange J_{ij}, equation (3.9) cannot be reduced to a function of $\mathbf{r}_i$–$\mathbf{r}_j$ and also depends on $\mathbf{R}_1$ and $\mathbf{R}_2$. The present model does not yield RKKY interactions in a proper sense, because shallow orbitals do not correspond to a sharp Fermi surface. However, aside from band-filling effects, the RKKY oscillation period π/k_F is essentially given by the interatomic distance. In the present model, the exchange changes sign in a very similar way, on a length scale given by the average distance between the donor and the acceptors.

The above mechanism is independent of whether the shallow orbitals form isolated clusters or percolate. In other words, it does not matter whether one considers dilute magnetic semiconductors or 'dilute magnetic dielectrics' [174]. However, the magnetic phase transition (critical temperature T_c) requires separate consideration. For localized spin-1/2 systems, the corresponding mean-field equation are

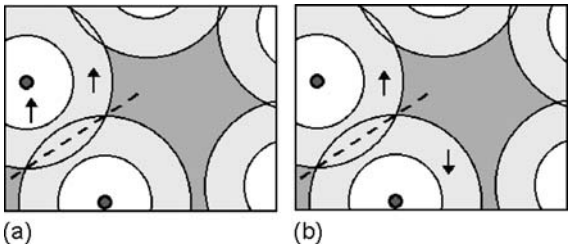

Fig. 3.14 Exchange mediated by two shallow orbitals: (**a**) ferromagnetic and (**b**) antiferromagnetic exchange. The *dark small circles* are the shallow donors or acceptors, whereas the *arrows* show the (fixed) positions of the localized 3d spins

$$m_i = \tanh\left(\frac{\Sigma_j J_{ij} m_j + \mu_o \mu_g H m_i}{k_B T}\right) \tag{3.10}$$

where $m_i = <S_i>$. At the critical point, the zero-field magnetization vanishes ($m_i = 0$) so that (6) can be linearized and $m_i = \Sigma_j J_{ij} m_j / k_B T$. This equation can also be written in secular form, $\Sigma_j (J_{ij} - k_B T \delta_{ij}) = 0$, indicating that the critical temperature is basically an eigenvalue of the matrix J_{ij}. In more detail, $k_B T_c = J_{max}$, where J_{max} is the largest eigenvalue of J_{ij}.[2] This procedure, applies to a wide range of materials, including ferro-, ferri-, and antiferromagnets [210]; spin glasses [183]; magnetic nanostructures [155]; and magnetic semiconductors [212]. The reliability

[2]The other eigenvalues have no transparent physical meaning, because $|m_i| > 0$ below T_c and the approximation $m_i = 0$ are no longer valid.

of the mean-field predictions depends on the dimensionality of the structure [155, 211] and on the range of the interactions, similar to the well-known critical behavior of homogenous magnets [86].

From a quantum-mechanical point of view, the RKKY theory is a fairly crude approximation. In particular, (3.7) ignores spin–orbit coupling, which affects the anisotropy and—to a lesser extend—the magnetization [207, 208]. Dilute magnetic semiconductors are often anisotropic, exhibiting not only a preferential magnetization direction but also a direction dependence of the magnetic moment, for example, in the film plane of V-doped SnO_2 [175].

3.4.3 Preasymptotic Coupling

Moment formation and interatomic exchange in itinerant magnets such as Fe, Co, and many of their alloys is very different from the coupling between stable local moments, as represented by the RKKY mechanism. Itinerant moments are strongly band-structure dependent, as epitomized by the Stoner criterion $ID(E_F) \geq 1$, where $I \sim 1$ eV is the Stoner parameter and $D(E_F)$ is the density of states (DOS) at the Fermi level. Small band widths $W \sim 1/D(E_F)$ favor ferromagnetism, because the intra-atomic interactions responsible for moment formation (I) compete against hybridization energies of order W.

Strongly exchange-enhanced Pauli paramagnets such as Pd and Pt, which nearly satisfy the Stoner criterion, are easily spin polarized by neighboring Fe or Co atoms. Examples are $L1_0$ magnets [176], Fe/Pt thin films [177], spin-glass-type dilute alloys [183], and various magnetic nanostructures [31, 135]. Some other elements such as V exhibit moderate exchange enhancement, whereas elements such as Cu and Ag can be considered as non-interacting metals [178]. The *spatial* aspect of exchange-enhanced Pauli paramagnetism is described by the wave-vector-dependent susceptibility [179]

$$\chi(k) = \frac{\chi_o(k)}{1 - U\chi_o(k)/2\mu_o{\mu_B}^2} \tag{3.11}$$

where $\chi_o(k)$ is the non-interacting or Pauli susceptibility:

$$\chi_o(k) = \chi_h(1 - k^2/12{k_F}^2 + O(k^2)) \tag{3.12}$$

The higher-order terms in this equation exhibit a complicated behavior with a singularity at $k = 2k_F$, which is the origin of the RKKY oscillations [164, 179]. However, when the Stoner criterion is nearly satisfied, the quadratic term is strongly enhanced in (3.11), and Fourier transformation yields a pronounced exponential decay with a decay length $1/\kappa$. The decay is preasymptotic, that is, for long distances there remains an oscillating tail [180]. For Pd thin films, the transition from exponential to power-law behavior occurs at about 10–12 monolayers [180]. The range of the preasymptotic decay scales as $1/(1 - UD)^{1/2}$. It is rarely larger than about 2 Å but

sufficient to spin polarize a significant neighborhood of atoms such as Pt or Pd. Figure 3.15 illustrates the geometry of the polarization cloud for small transition-metal dots on a 4d/5d surface.

For semiquantitative calculation of polarization-cloud and interdot exchange coupling (Fig. 3.15), it is convenient to start from the energy density [181, 182]

$$\eta = \frac{1}{48{k_\mathrm{F}}^2 D}(\nabla m)^2 + \frac{1}{4}\left(\frac{1}{D} - U\right)m^2 \tag{3.13}$$

By Fourier transformation, it is straightforward to show that this equation corresponds to the quadratic limit of (3.11). Minimization of (3.13) yields the Yukawa-type equation $\nabla^2 m + \kappa^2 m = 0$. Let us first consider a spherical Fe or Co particle of radius R_o in a Pt or Pd matrix. In this case, the Yukawa equation with the well-known spherical solution $m_\mathrm{s}(r) = c\,\exp(-\kappa r)/4\pi r$, where r is the distance from the center of the cluster. Next, we integrate $m(\mathbf{r})$ over $4\pi r^2 \mathrm{d}r$, taking into account that the magnetization at the cluster surface is equal to that of the Fe or Co, $m(R) = m_\mathrm{o}$, and that the moment of the Fe particle $\mu_\mathrm{o} = 4\pi {R_\mathrm{o}}^3 m_\mathrm{o}/3$. This yields the moment

$$\mu = 3\mu_\mathrm{o}\frac{1 + \kappa R_\mathrm{o}}{\kappa^2 {R_\mathrm{o}}^2} \tag{3.14}$$

Taking a single Co atom of moment $\mu_\mathrm{o} = 1.73\ \mu_\mathrm{B}$ and radius $R = 1.24$ Å, we obtain theoretical polarization-cloud predictions of about 3.5 μ_B for Pt and 7.3 μ_B for Pd. Moments of this order of magnitude are indeed observed, for example, in dilute alloys [183].

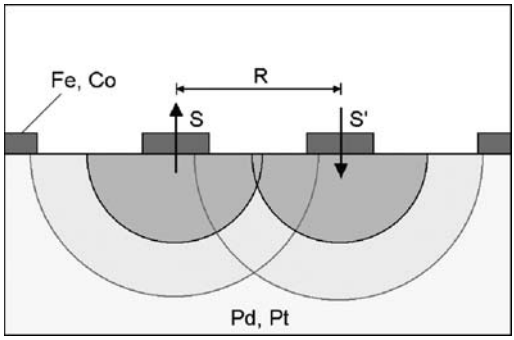

Fig. 3.15 Coupling between two Fe or Co clusters on a Pt surface (schematic). The exchange is estimated by volume integration of the energy density (3.13), thereby ignoring surface-state contributions

The interdot exchange $J = -(E_+ - E_-)$ is obtained by putting $m_\pm(\mathbf{r}) \sim m_\mathrm{s}(|\mathbf{r} - \mathbf{R}_1|) \pm m_\mathrm{s}(|\mathbf{r} - \mathbf{R}_2|)$ into (3.13) and evaluating the total energies $E_\pm = \int \eta(m_\pm)\,\mathrm{d}V$. Here the sign corresponds to ferromagnetic (+) and antiferromagnetic (−) exchange, and the calculation requires careful bookkeeping, including the boundary condition $m_\pm(\mathbf{r}) = m_\mathrm{o}$ at the cluster−matrix interface and the consideration of the semi-infinite character of the problem [99] and yields in lowest order

$$J = \frac{J_{\mathrm{at}}}{2} \frac{{R_{\mathrm{o}}}^2}{{R_{\mathrm{at}}}^2} \exp(-\kappa R) \tag{3.15}$$

Equation (3.15) shows that the exchange increases quadratically with the radius R of the clusters but is rapidly outweighed by the exponential term. This is different from the RKKY interaction between nanoparticles [165], which exhibits a power-law dependence on the particle or cluster separation. Taking $R_{\mathrm{o}} = 1\,\mathrm{nm}$ and $R = 3\,\mathrm{nm}$ yields an effective preasymptotic interaction of about 5 mK, corresponding to an interaction field of order 15 μT. By comparison, magnetostatic interaction fields are typically of the order of a few mT. In other words, for cluster sizes and separations exceeding about 1 nm, intercluster interactions are weaker than magnetostatic dipole interactions and the RKKY tail interactions through the substrate.

3.4.4 Kondo Effect

The Kondo effect arises when electrons of a spatially confined system with discrete energy levels interact with the conduction electrons of an otherwise non-magnetic metal. Such systems can be ferromagnetic impurities in strongly diluted alloys, or magnetic adatoms, clusters, magnetic molecules, or artificial quantum structures on metal surfaces (recent reviews in [184, 185]). Requirements for the Kondo effect to occur are that the defects are magnetic, that is, they have a nonzero total spin, and that the metal is cooled to temperatures below the Kondo temperature, T_{K}. At the origin of the Kondo effect are correlated electron exchange processes between the discrete and continuum states that effectively flip the spin of the impurity, while simultaneously creating a spin excitation in the Fermi sea (see Fig. 3.16). The involved electrons form a many-electron ground state, the Kondo state. The Kondo temperature can be thought of as the binding energy of this correlated state and is typically of the order of 0−400 K. The spin polarization of the impurity and the host are opposite to each other, hence, the conduction electrons effectively screen the impurity's spin.

The Kondo effect has two profound experimental consequences: (i) the magnetization is reduced below the free-moment value due to the screening, and (ii) the electron scattering cross-section of the impurity is strongly enhanced, resulting in anomalies in transport measurements near and below T_{K}. The Kondo resonance is experimentally observable on surface-supported atoms or nanostructures with low-temperature scanning tunneling microscopy (STM), where it shows up as a Fano resonance in the differential conductance of the tunneling contact $\mathrm{d}I/\mathrm{d}V$ at the lateral adatom position [186–189].

Progress in nanotechnology has made it possible to construct spatially confined nanostructures with pronounced discretization of electronic states, in which the Kondo physics is clearly displayed [190–192]. The Kondo effect is thus by no means limited to single impurity atoms but is a phenomenon generally associated

with magnetic nanoscale systems with discrete electronic states and non-zero net spin. However, the Kondo temperature is rapidly suppressed as the size of the cluster increases and goes to zero exponentially with increasing cluster size [193]. The Kondo effect is of fundamental importance for the study of magnetism in nanoscale systems, as it can serve as a local probe to determine the exchange interaction in sub-nanometer clusters. For instance, the magnetic ground state of spin-frustrated Cr trimers [194] and the exchange interaction between single Ni or Co atoms [195, 196] could be determined from measurements of the Kondo state the clusters form with the substrate. Recent experiments have demonstrated that the Kondo effect can be manipulated by tuning the interaction with the bulk-state electrons via local coordination, chemical bonding, or quantum size effects [197–199].

Potential applications for the Kondo effect might arise in spintronics and quantum information processing, as it permits, for example, to transport information in systems which are too small for conventional wiring [191].

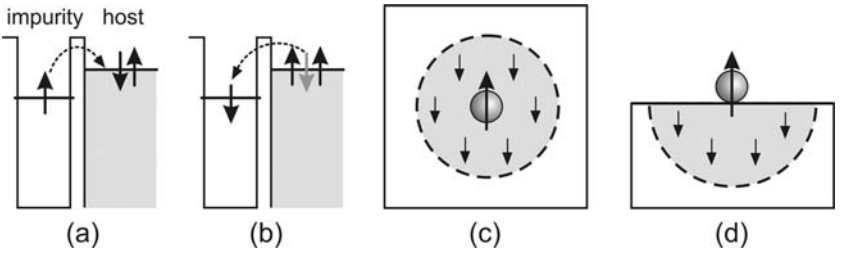

Fig. 3.16 Electronic (spin-flip) exchange between the discrete energy levels of an impurity and the delocalized states of a host metal, leading to the Kondo effect. An electron tunnels into an empty state near the Fermi energy of the host (**a**), and the hole is filled with an electron of opposite spin from the host (**b**). The so-induced spin polarization of the delocalized electrons around the impurity is effectively screening the magnetic moment of the impurity. (**c**) Screening cloud around an impurity in a bulk matrix and (**d**) on a metal surface

3.4.5 Entanglement

Entanglement is a key consideration in quantum information processing systems [200–203], including magnetic nanostructures [158]. It has been shown theoretically that and how quantum entanglement arises in interacting magnetic nanodots [158]. The thermal stability of the entangled states increases with the magnetic anisotropy of the dots, which reaches substantial values for some noncubic intermetallic compounds. This is of potential importance for future quantum computing above 4.2 K.

An example of an entangled state is the wave function $|\Phi> = |\alpha> |\beta> + |\beta> |\alpha>$, which cannot be written as a product of one-electron states. Entanglement between magnetic nanodots of total spin S can be realized by using the macrospin wave functions of the type $|\alpha> = |S>$ and $|\beta> = |S - 1>$. Another approach is

to exploit those wave functions such as $|\Phi>$, which naturally occur in Heisenberg magnets. Fig. 3.17 shows a simple example, namely the AFM spin-1/2 Heisenberg square. The square is described by the transparent Hamiltonian

$$\mathrm{H} = -J(\mathbf{s}_1 \cdot \mathbf{s}_2 + \mathbf{s}_2 \cdot \mathbf{s}_3 + \mathbf{s}_3 \cdot \mathbf{s}_4 + \mathbf{s}_4 \cdot \mathbf{s}_1) \tag{3.16}$$

where $J > 0$. The quantum states of the square may be manipulated by an inhomogeneous magnetic field and/or by interactions with neighboring dots.

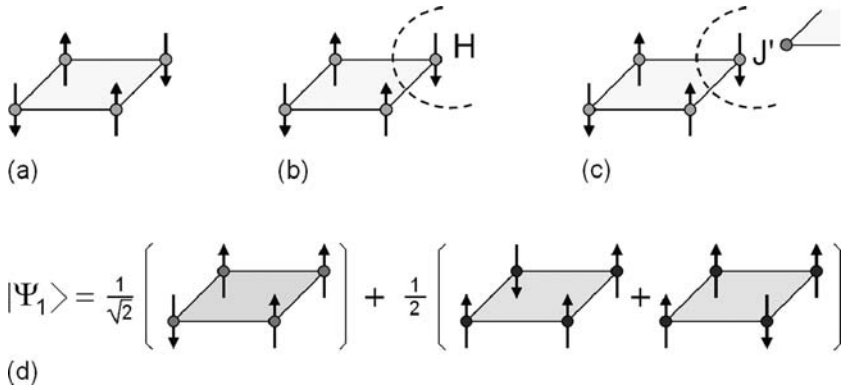

Fig. 3.17 Interactions and entanglement in small-scale nanostructures: (**a**) free square, (**b**) local interaction field, (**c**) exchange interaction with neighboring atoms, and (**d**) entangled wave function in the limit of strong interactions. For simplicity, only the ground state is shown in (**d**)

In spite of its simplicity, the model exhibits a substantial degree of complexity, even in the ground state. In the absence of a magnetic field, the classical ground state is shown in Fig. 3.17a, meaning that neighboring spins minimize the energy by forming pairs with antiparallel spins. The quantum-mechanical ground state is of the many-electron type but easily obtained by diagonalizing the 16×16 Hamilton matrix (3.4). Aside from the classical ground-state configurations, Fig. 3.17a, there is a substantial admixture of states that have two parallel bonds, as in Fig. 3.17b. These states do not appear in the classical ground state, because they cost exchange energy, but in the quantum-mechanical case, they reduce the total energy by realizing hybridization between degenerate classical ground-state configurations.

From a quantum-mechanical point of view, Heisenberg spin structures are highly complicated and poorly described by one-electron approaches, including LSDA+U and SIC. A particular effect is spin-charge separation, meaning that the low-lying excitations are magnetic and rather unrelated to the interatomic hopping of the electrons [179, 204]. In more detail, the Heisenberg model assumes that the four spin-carrying electrons are localized at the corners of the square but the spins are free to switch. The electron's interatomic hopping (hopping integral t) is important in itinerant and RKKY systems but enters the Heisenberg model only indirectly by determining the exchange [179].

3.5 Concluding Remarks

In summary, we have investigated how nanoscale proximity effects change the properties of magnetic nanostructures. Progress in fabrication and deposition techniques has made it possible to produce an unprecedented range of structures, from embedded and coated clusters to nanotubes and complex thin films, including magnetic surface alloys. The structures offer new physics on length scales of more than a few interatomic distances, making it different from typical atomic-environment effects in alloys and at surfaces. Focus has been on the relation between classical and quantum effects. Some quantum effects, such as RKKY interactions between nanoparticles, but many nanoscale effects are of the micromagnetic type, where interatomic exchange ensures a coherent spin orientation over several nanometers. An example of the latter is proteresis in core–shell nanoparticles, which is counterintuitive from a magnetostatic point of view but explained by the involvement of nanoscale exchange interactions between noncollinear magnetic sublattices. While future research is necessary in various directions, including, for example, the fabrication of monodisperse metal clusters on substrates with good control over size, density, orientation, and anisotropy, the structures will have potential applications in many areas of nanotechnology, from biomagnetism and sensors to materials for bulk applications and structures for quantum and classical information processing. It will be fascinating to monitor and accompany this development in the years to come.

Acknowledgments The contribution of A.E. to this work was supported by NSF CAREER (DMR-0747704), that of R.S. by DoE, and D.J.S. by NSF-MRSEC and INSIC. The authors havebenefited from discussions with X.-H. Wei, R. D. Kirby, S. A. Michalski, S. Enders, J. Zhang, R. Zhang, J. Zhou (Nebraska), and J. Honolka, J. Zhang, V. Sessi, I. Brihuega, and K. Kern (Stuttgart).

References

1. Feynman, R. P.: There's plenty of room at the bottom. Eng. Sci. **23**, 22 (1960)
2. Solzi, M., et al.: Macroscopic Magnetic Properties of Nanostructured and Nanocomposites Systems. In H. S. Nalwa (Ed.), Magnetic nanostructures, pp. 123–201. American Scientific, Stephenson Ranch (2002)
3. Skomski, R.: Nanomagnetics. J. Phys.: Condens. Matter **15**, R841 (2003)
4. Sellmyer, D. J. and Skomski, R. (Eds.): Advanced Magnetic Nanostructures. Springer, Berlin (2006)
5. Terris, B. D., et al.: Ion-beam patterning of magnetic films using stencil masks. Appl. Phys. Lett. **75**, 403 (1999)
6. Coehoorn, R., et al.: Meltspun permanent magnet materials containing Fe_3B as the main phase. J. Magn. Magn. Mater. **80**, 101 (1989)
7. Toshima, N., et al.: Novel synthesis, structure and catalysis of inverted core/shell structured Pd/Pt bimetallic nanoclusters. Eur. Phys. J. D **16**, 209 (2001)
8. Wei, X.-H., et al.: Proteresis in Co:CoO core-shell nanoclusters. J. Appl. Phys. **103**, 07D514-1-3 (2008)
9. Khanna, S. N., et al.: Magic numbers in metallo-inorganic clusters: chromium encapsulated in silicon cages. Phys. Rev. Lett. **89**, 016803-1-4 (2002)

10. Bland, J. A. C. and Heinrich, B. (Eds.): Ultrathin Magnetic Structures I. Springer, Berlin (2005)
11. Himpsel, F. J., et al.: Magnetic nanostructures. Adv. Phys. **47**, 511 (1998)
12. Sawicki, M., et al.: Exchange springs in antiferromagnetically coupled DyFe2-YFe2 superlattices. Phys. Rev. B **62**, 5817 (2000)
13. Al-Omari, A. and Sellmyer, D. J.: Magnetic properties of nanostructured CoSm/FeCo films. Phys. Rev. B **52**, 3441 (1995)
14. Sellmyer, D. J.: Applied physics: strong magnets by self-assembly. Nature **420**, 374 (2002)
15. Zeng, H., et al.: Curie temperature of FePt:B_2O_3 nanocomposite films. Phys. Rev. B **66**, 184425 (2002)
16. Sellmyer, D. J., et al.: Nanoscale design of films for extremely high density magnetic recording. Phys. Low-Dim. Struct. **1–2**, 155 (1998)
17. Rao, B. K. and Jena, P.: Giant magnetic moments of nitrogen-doped Mn clusters and their relevance to ferromagnetism in Mn-Doped GaN. Phys. Rev. Lett. **89**, 185504 (2002)
18. Sui, Y. C., et al.: Nanotube magnetism. Appl. Phys. Lett. **84**, 1525 (2004)
19. Kumar, K.: $RETM_5$ and RE_2TM_{17} permanent magnets development. J. Appl. Phys. **63**, R13–57 (1988)
20. Zhou, J., et al.: Sm-Co-Ti high-temperature permanent magnets. Appl. Phys. Lett. **77**, 1514 (2000)
21. Wernsdorfer, W., et al.: Macroscopic quantum tunneling of magnetization of single ferrimagnetic nanoparticles of barium ferrite. Phys. Rev. Lett. **79**, 4014 (1997)
22. Rong, Ch.-B., et al.: Structural phase transition and ferromagnetism in monodisperse 3 nm FePt particles. J. Appl. Phys. **101**, 043913-1-4 (2007)
23. Skomski, R. and Coey, J. M. D.: Giant energy product in nanostructured two-phase magnets. Phys. Rev. B **48**, 15812 (1993)
24. Samorjai, G. A.: Introduction to Surface Chemistry and Catalysis. Wiley, New York (1994)
25. Wieckowski, A., Savinova, E. R. and Constantinos, V. G. (Eds.): Catalysis and Electrocatalysis at Nanoparticle Surfaces. Marcel Dekker, New York (2003)
26. Skomski, R. and Sellmyer, D. J.: Magnetic impurities in magic-number clusters.
27. Pankhurst, Q. A., et al.: J. Phys. D: Appl. Phys. **36**, R167–R181 (2003).
28. Sun, S., et al.: Monodisperse FePt nanoparticles and ferromagnetic FePt nanocrystal superlattices. Science **287**, 1989 (2000)
29. Weller, D., et al.: High Ku materials approach to 100 Gbits/in^2. IEEE Trans. Magn. **36**, 10 (2000)
30. Billas, I. M. L., et al.: Magnetism from the atom to the bulk in Iron, Cobalt, and Nickel clusters. Science **265**, 1682 (1994)
31. Stepanyuk, V. S., et al.: Magnetism of 3d, 4d, and 5d transition-metal impurities on Pd(001) and Pt(001) surfaces. Phys. Rev. B **53**, 2121 (1996)
32. Pastor, M., et al.: Magnetic anisotropy of 3d transition-metal clusters. Phys. Rev. Lett. **75**, 2, 326 (1995)
33. Nonas, B., et al.: Strongly enhanced orbital moments and anisotropies of adatoms on the Ag(001) surface. Phys. Rev. Lett. **86**, 10, 2146 (2001)
34. Goldoni, A., et al.: Experimental evidence of magnetic ordering at the Rh(100) surface. Phys. Rev. Lett. **82**, 15, 3156 (1999)
35. Martin, T. P.: Shells of atoms. Phys. Rept. **273**, 199 (1996)
36. Heiz, U., et al.: Size-dependent molecular dissociation on mass-selected, supported metal clusters. J. Am. Chem. Soc. **120**, 9668 (1998)
37. Lee, H. K., et al.: Monte Carlo simulations of interacting magnetic nanoparticles. J. Appl. Phys. **91**, 10, 6926 (2002)
38. Pierce, J. B., et al.: Ferromagnetic stability in Fe nanodot assemblies on Cu(111) induced by indirect coupling through the substrate. Phys. Rev. Lett. **92**, 23, 237201 (2004)
39. Dürr, H. A., et al.: Spin and orbital magnetization in self-assembled Co clusters on Au(111). Phys. Rev. B **59**, 2, R701 (1999)

40. Fruchart, O., et al.: Enhanced coercivity in submicrometer-sized ultrathin epitaxial dots with in-plane magnetization. Phys. Rev. Lett. **82**, 6, 1305 (1999)
41. Edmonds, K. W., et al.: Doubling of the orbital magnetic moment in nanoscale Fe clusters. Phys. Rev. B **60**, 1, 472 (1999)
42. Guevara, J., et al.: Large variations in the magnetization of Co clusters induced by noble-metal coating. Phys. Rev. Lett. **81**, 24, 5306 (1998)
43. Redinger, J., et al.: Ferromagnetism of 4d and 5d transition-metal monolayers on Ag(111). Phys. Rev. B **51**, 19, 13852 (1995)
44. Allwood, D. A., et al.: Nanoscale magnetics magnetic domain wall logic. Science **309**, 1688 (2005)
45. Sorge, K. D., et al.: Interactions and switching behavior of anisotropic magnetic dots. J. Appl. Phys. **95**, 7414 (2004)
46. Weller, D. and Moser, A.: Thermal effect limits in ultrahigh density magnetic recording. IEEE Trans. Magn. **35**, 4423 (1999)
47. Suess, D., et al.: Exchange spring media for perpendicular recording. Appl. Phys. Lett. **87**, 012504 (2005)
48. Suess, D.: Multilayer exchange spring media for magnetic recording. Appl. Phys. Lett. **89**, 113105-1-3 (2006)
49. Victora, R. H. and Shen, X.: Composite media for perpendicular magnetic recording. IEEE Trans. Magn. **41**, 537 (2005)
50. Sellmyer, D. J., et al.: High-anisotropy nanocomposite films for magnetic recording. IEEE Trans. Magn. **37**, 1286 (2001)
51. Wang, J.-P., et al.: Composite media (dynamic tilted media) for magnetic recording. Appl. Phys. Lett. **86**, 142504-1-3 (2005)
52. Goodman, S. J., et al.: Micromagnetics of hysteresis loops in CGC perpendicular media. IEEE Trans. Magn. **39**, 2329 (2003)
53. Dobin, A. Yu., et al.: Domain wall assisted magnetic recording. Appl. Phys. Lett. **89**, 062512-1-3 (2006)
54. Baettig, P., et al.: Ab initio prediction of a multiferroic with large polarization and magnetization. Appl. Phys. Lett. **86**, 012505-1-3 (2005)
55. Barth, J. V., et al.: Engineering atomic and molecular nanostructures at surfaces. Nature **437**, 671 (2005)
56. Wang, F. and Lakhtakia, A. (Eds.): Selected Papers on Nanotechnology—Theory and Modeling, Milestone Series **182**. SPIE Press, Bellingham (2006)
57. Skomski, R., et al.: Micromagnetics of ultrathin films with perpendicular magnetic anisotropy. Phys. Rev. B **58**, 3223 (1998)
58. Skomski, R.: Nanomagnetic scaling. J. Magn. Magn. Mater. **272–276**, 1476–1481 (2004)
59. Skomski, R.: Role of thermodynamic fluctuations in magnetic recording. J. Appl. Phys. **101**, 09B104-1-6 (2007)
60. Qiang, Y., et al.: Magnetism of Co nanocluster films. Phys. Rev. B **66**, 064404 (2002)
61. Sellmyer, D. J., et al.: Magnetism of Fe, Co and Ni nanowires in self-assembled arrays. J. Phys.: Condens. Matter **13**, R433–R460 (2001)
62. Liou, S. H. and Yao, Y. D.: Development of high coercivity magnetic force microscopy tips. J. Magn. Magn. Mater. **190**, 130 (1998)
63. Kent, A. D., et al.: Properties and measurement of scanning tunneling microscope fabricated ferromagnetic particle arrays. J. Appl. Phys. **76**, 6656 (1994)
64. Xu, Y. F., et al.: Cluster-Assembled Nanocomposites. In D. J. Sellmyer and R. Skomski (Eds.), Advanced magnetic nanostructures, ch. 8, pp. 207–238. Springer, Berlin (2006)
65. Enders, A., et al.: Magnetism of low-dimensional metallic structures. In H. Kronmüller and S. Parkin (Eds.), The handbook of magnetism and advanced magnetic materials, Vol. 1: Fundamentals and theory, pp. 577–598. Chichester, UK: John Wiley & Sons Ltd. (2006)
66. Barth, J. V.: Molecular architectonic on metal surfaces. Annu. Rev. Phys. Chem. **58**, 375 (2007)

67. Gambardella, P., et al.: Ferromagnetism in one-dimensional monatomic metal chains. Nature **416**, 301 (2002)
68. Repetto, D., et al.: Structure and magnetism of atomically thin Fe layers on flat and vicinal Pt surfaces. Phys. Rev. B **74**, 054408 (2006)
69. Skomski, R. and Coey, J. M. D.: Permanent Magnetism. Institute of Physics, Bristol (1999)
70. Skomski, R., et al.: Effective Demagnetizing Factors of Complicated Particle Mixtures. IEEE Trans. Magn. **43**, (6), 2956 (2007)
71. Zhang, J., et al.: Magnetism of Fe clusters formed by buffer-layer assisted growth on Pt(997). Eur. Phys. J. D **45**, 515 (2007)
72. Rusponi, S., et al.: The Remarkable Difference Between Surface and Step Atoms in the Magnetic Anisotropy of Two-Dimensional Nanostructures. Nature Mat. **2**, 546 (2003)
73. Brihuega, I., et al.: Electronic decoupling and templating of Co nanocluster arrays on the boron nitride nanomesh. Surf. Sci. Letters 602(14) (2008) L95–L99.
74. Lingenfelder, M., et al.: Towards surface-supported supramolecular architectures: tailored coordination assembly of 1,4-benzenedicarboxylate and Fe on Cu(100). Chem. Eur. J. **10**, 1913 (2004)
75. Dmitriev, A., et al.: Design of extended surface-supported chiral metal-organic arrays comprising mononuclear iron centers. Langmuir **41**, 4799 (2004)
76. Bromann, K., et al.: Controlled deposition of size-selected Silver nanoclusters. Science **274**, 956 (1996)
77. Weaver, J. and Waddill, G.: Cluster assembly of interfaces: Nanoscale Engineering. Science **251**, 1444 (1991), G. Kerner and M. Asscher, "Laser patterning of metallic films via buffer layer", ibid.
78. Huang, L., et al.: Buffer-layer-assisted growth of nanocrystals: Ag-Xe-Si(111). Phys. Rev. Lett. **80**, 18, 4095 (1998)
79. Haley, C. and Weaver, J.: Buffer-layer-assisted nanostructure growth via two-dimensional cluster–cluster aggregation. Surf. Sci. **518**, 243 (2002)
80. Weaver, J. and Antonov, V. N.: Synthesis and patterning of nanostructures of (almost) anything on anything. Surf. Sci. **557**, 1 (2004)
81. Hahn, E., et al.: Orientational instability of vicinal Pt surfaces close to (111). Phys. Rev. Lett., **72** 3378 (1994)
82. Corso, M., et al.: Boron nitride nanomesh. Science **303**, 217 (2004)
83. Bansmann, J., et al. : Magnetic and structural properties of isolated and assembled clusters. Surf. Sci. Repts. **56**, 189 (2005)
84. Shen, J., et al.: The effect of spatial confinement on magnetism: films, stripes and dots of Fe on Cu(111). J. Phys.: Cond. Mat. **15**, R1 (2003)
85. Repetto, D., et al.: Magnetism of Fe clusters and islands on Pt surfaces. Appl. Phys. A **82**, 109 (2006)
86. Yeomans, J. M.: Statistical Mechanics of Phase Transitions. University Press, Oxford (1992)
87. Yokoyama, T., et al.: Selective assembly on a surface of supramolecular aggregates with controlled size and shape. Nature **413**, 619 (2001)
88. Grill, L., et al.: Nano-architectures by covalent assembly of molecular building blocks. Nat. Nanotech. **2**, 687 (2007)
89. Dmitriev, A., et al.: Modular assembly of two-dimensional metal-organic coordination networks at a metal surface. Angew. Chem. Int. Ed. **42**, 2670 (2003)
90. Stepanow, S., et al.: Steering molecular organization and host-guest interactions using two-dimensional nanoporous coordination systems. Nat. Mater. **3**, 229 (2004)
91. Ruben, M., et al.: 2D supramolecular assemblies of Benzene 1,3,5-tri-yl Tribenzoic Acid: Temperature-induced phase transformations and hierarchical organization with macrocyclic molecules. J. Am. Chem. Soc. **128**, 15644 (2006)
92. Hauschild, A., et al.: Molecular distortions and chemical bonding of a large π-conjugated molecule on a metal surface. Phys. Rev. Lett. **94**, 036106 (2005)

93. Boehringer, M., et al.: Two-dimensional self-assembly of supramolecular clusters and chains. Phys. Rev. Lett. **83**, 324 (1999)
94. Klemmer, T., et al.: Magnetic hardening and coercivity in $L1_0$ Ordered FePd ferromagnets. Scripta Met. Mater. **33**, 1793 (1995)
95. T.-Lee, et. al.: Growth and surface alloying of Fe on Pt(997). Surf. Sci. **600**, 3266 (2006)
96. Ravindran, P., et al.: Large magnetocrystalline anisotropy in bilayer transition metal phases from first-principles full-potential calculations Phys. Rev. B **63**, 144409-1-18 (2001)
97. Komelj, M., et al.: Influence of the substrate on the magnetic anisotropy of monatomic nanowires. Phys. Rev. B **73**, 134428 (2006)
98. Lee, T.-Y., et al.: Growth and surface alloying of Fe on Pt(997). Surf. Sci. **600** (16) 3266 (2006)
99. Skomski, R., et al.: Substrate-controlled growth and magnetism of nanosize Fe clusters on Pt. J. Appl. Phys. **103**, 07D519-1-3 (2008)
100. Ising E.: Beitrag zur Theorie des Ferromagnetismus. Z. Phys. **31**, 253 (1925)
101. De Jongh, L. J. and Miedema, A. R.: Experiments on simple magnetic model systems. Advan. Phys. **23**, 1 (1974)
102. Shen, J., et al.: Magnetism in one dimension: Fe on Cu(111). Phys. Rev. B **56**, 2340 (1997)
103. Alefeld, G.: Wasserstoff in Metallen als Beispiel für ein Gittergas mit Phasenumwandlungen. Phys. stat. sol. **32**, 67 (1969)
104. Wagner, H. and Horner, H.: Elastic interaction and the phase transition in coherent metal-hydrogen system. Adv. Phys. **23**, 587 (1974)
105. Skomski, R.: Interstitial Modification, In J. M. D. Coey (Ed.), Rare-earth—iron permanent magnets, pp. 178–217. University Press, Oxford (1996)
106. Wood, R.: The feasibility of magnetic recording at 1 Terabit per square inch. IEEE Trans. Magn. **36**, 36 (2000)
107. Sellmyer, D. J., et al.: High-anisotropy nanocomposite films for magnetic recording. IEEE Trans. Magn. **37**, 1286 (2001)
108. McCurrie, R. A. and Gaunt, P.: The magnetic properties of platinum-cobalt near the equiatomic composition. I. The experimental data. Philos. Mag. **13**, 567 (1966)
109. Zeng, H., et al.: Orientation-controlled nonepitaxial L10 CoPt and FePt films. Appl. Phys. Lett. **80**, 2350 (2002)
110. Yan, M. L. et al.: Fabrication of nonepitaxially grown double-layered FePt:C/FeCoNi thin films for perpendicular recording. Appl. Phys. Lett. **83**, 3332 (2003)
111. Xu, Y., et al.: Magnetic properties of dilute FePt:C nanocluster films. J. Appl. Phys. **97**, 10J320 (2005)
112. Xu, Y., et al.: Magnetic properties of L10 FePt and FePt:Ag nanocluster films. J. Appl. Phys. **93**, 10 (2003) 8289
113. Stoner, E. C. and Wohlfarth, E. P.: A mechanism of magnetic hysteresis in heterogeneous alloys. Philos. Trans. R. Soc. London, Ser. A **240**, 599 (1948); reprinted by IEEE Trans. Magn. **27**, 3475 (1991)
114. Kersten, M.: Zur Theorie der ferromagnetischen Hysterese und der Anfangspermeabilität. Z. Phys. **44**, 63 (1943)
115. Yoshizawa, Y., et al.: New Fe-based soft magnetic alloys composed of ultrafine grain structure. J. Appl. Phys. **64**, 6044 (1988)
116. Herzer, G.: Nanocrystalline soft magnetic materials. J. Magn. Magn. Mater. **112**, 258 (1992)
117. Chikazumi, S., Physics of ferromagnetism, Second edition. Oxford University Press, (1997)
118. Kittel, Ch.: Theory of the structure of ferromagnetic domains in films and small particles. Phys. Rev. **70**, 965 (1946)
119. Kronmüller, H. and Schrefl, T.: Interactive and cooperative magnetization processes in hard magnetic materials. J. Magn. Magn. Mater. **129**, 66 (1994)
120. Skomski, R.: Simple Models of Magnetism. University Press, Oxford (2008)

121. Skomski, R., et al.: Magnetization reversal in cubic nanoparticles with uniaxial surface anisotropy. IEEE Trans. Magn. **43**, (6), 2890 (2007)
122. Kronmüller, H.: Theory of nucleation fields in inhomogeneous ferromagnets. Phys. Stat. Sol. (b) **144**, 385 (1987)
123. Nieber, S. and Kronmüller, H.: Nucleation fields in periodic multilayer's. Phys. Stat. Sol. (b) **153**, 367 (1989)
124. Kneller, E. F. and Hawig, R.: The exchange-spring magnet: a new material principle for permanent magnets. IEEE Trans. Magn. **27**, 3588 (1991)
125. Gradmann, U.: In Handbook of Magnetic Materials Vol. 7, In K. H. J. Buschow (Ed.), Elsevier Science Publishers B. V., New York, (1993)
126. Kachkachi, H. and Bonet, E.: Surface-induced cubic anisotropy in nanomagnets. Phys. Rev. B **73**, 224402-1-7 (2006)
127. Komelj, M., et al.: From the bulk to monatomic wires: An ab initio study of magnetism in Co systems with various dimensionality. Phys. Rev. B **66**, 140407-1-4 (2002)
128. Daalderop, G. H. O., et al.: First-principles calculation of the magnetic anisotropy energy of (Co)n/(X)m multilayers. Phys. Rev. B **42**, 11, 7270 (1990)
129. Wang, D.-Sh., et al.: First-principles theory of surface magnetocrystalline anisotropy and the diatomic-pair model. Phys. Rev. B **47**, 14932 (1993)
130. Skomski, R.: Exchange-Controlled Magnetic Anisotropy. J. Appl. Phys. **91**, 8489 (2002)
131. Sander, D., et al.: Reversible H-induced switching of the magnetic easy axis in Ni/Cu(001) thin films. Phys. Rev. Lett. **93**, 247203-1-4 (2004)
132. Brooks, H.: Ferromagnetic anisotropy and the itinerant electron model. Phys. Rev. **58**, 909 (1940)
133. Sander, D., et al.: Film stress and domain wall pinning in sesquilayer iron films on W(110). Phys. Rev. Lett. **77**, 2566 (1996)
134. Morales, M. A., et al.: Surface anisotropy and magnetic freezing of MnO nanoparticles. Phys. Rev. B **75**, 134423 (1–5) (2007)
135. Gambardella, P., et al.: Giant magnetic anisotropy of single cobalt atoms and nanoparticles. Science **300**, 1130 (2003)
136. Ŝipr, O., et al.: Magnetic structure of free iron clusters compared to iron crystal surfaces. Phys. Rev. B **70**, 174423 (2004)
137. Kechrakos, D. and Trohidou, K.: Magnetic properties of dipolar interacting single-domain particles. Phys. Rev. B **58**, 12169 (1998)
138. Novosad, V., et al. : Effect of interdot magnetostatic interaction on magnetization reversal in circular dot arrays. Phys. Rev. B **65**, 60402 (2002)
139. Stepanyuk, V. S., et al.: Magnetism of 3d, 4d, and 5d transition-metal impurities on Pd(001) and Pt(001) surfaces. Phys. Rev. B **53**, 2121(1996)
140. Ederer, C., et al.: Magnetism in systems with various dimensionalities: A comparison between Fe and Co. Phys. Rev. B **68**, 52402 (2003)
141. Garibay-Alonso, R. and López-Sandoval, R.: Ground-state spin local magnetic moments of deposited Fe clusters Solid State Comm. **134**, 503 (2005)
142. Skomski, R., et al.: Finite-temperature anisotropy of PtCo magnets. IEEE Trans. Magn. **39**, 2917 (2003)
143. Mryasov, O. N., et al.: Temperature-dependent magnetic properties of FePt: Effective spin Hamiltonian model. Europhys. Lett. **69**, 805 (2005)
144. Skomski, R., et al.: Finite-temperature anisotropy of magnetic alloys. J. Appl. Phys. **99**, 08E916-1-4 (2006)
145. Tserkovnyak, Y., et al.: Enhanced Gilbert damping in thin ferromagnetic films. Phys. Rev. Lett. **88**, 117601-1-4 (2002)
146. Chipara, M. I., et al.: Magnetic modes in Ni nanowires. J. Magn. Magn. Mater. **249**, 246 (2002)
147. Skomski, R., et al: Incoherent magnetization reversal in nanowires. J. Magn. Magn. Mater. **249**, 175 (2002)

148. McMichael, R. D., et al.: Localized ferromagnetic resonance in inhomogeneous thin films. Phys. Rev. Lett. **90**, 227601-1-4 (2003)
149. Andersen, T., et al.: Substrate effects on surface magnetism of Fe/W(110) from first principles. Phys. Rev. B **74**, 184415-1-8 (2006)
150. Kashyap, A., et al.: Magnetism of $L1_0$ compounds with the composition MT (M = Rh, Pd, Pt, Ir and T = Mn, Fe, Co, Ni). J. Appl. Phys. **95**, 7480 (2004)
151. Umetsu, R. Y., et al.: Magnetic anisotropy energy of antiferromagnetic $L1_0$-type equiatomic Mn alloys. Appl. Phys. Lett. **89**, 052504-1-3 (2006)
152. Willoughby, S., et al.: Electronic, Magnetic and Structural Properties of $L1_0$ $FePt_xPd_{1-x}$ Alloys. J. Appl. Phys. **91**, 8822 (2002)
153. McHenry, M. E., et al.: First principles calculations of the electronic structure of $Fe_{1-x}Co_xPt$ IEEE Trans. Mag. **37**, 1277 (2001)
154. Skomski, R.: Phase formation in $L1_0$ magnets. J. Appl. Phys. **101**, 09N517-1-3 (2007)
155. Skomski, R. and Sellmyer, D.J.: Curie Temperature of Multiphase Nanostructures. J. Appl. Phys. **87**, 4756 (2000)
156. Evetts, J. E. (Ed.): Concise Encyclopedia of Magnetic and Superconducting Materials, Pergamon, Oxford, (1992)
157. O'Shea, M. J. and Al-Sharif, A. L.: Inverted hysteresis in magnetic systems with interface exchange. J. Appl. Phys. **75**, 6673 (1994)
158. Skomski, R., et al.: Quantum entanglement of anisotropic magnetic nanodots. Phys. Rev. A **70**, Art. No. 062307-1-4 (2004)
159. Tejada, J., et al.: Macroscopic resonant tunneling of magnetization in ferritin. Phys. Rev. Lett. **79**, 1754 (1997);
160. Lambrecht, W. R. L. and Andersen, O. K.: Minimal basis sets in the linear muffin-tin orbital method: Application to the diamond-structure crystals C, Si, and Ge. Phys. Rev. B **34**, 2439 (1986)
161. Tank, R. W. and Arcangeli, C.: An introduction to the third-generation LMTO method. Phys. Stat. Sol. (b) **217**, 89 (2000)
162. Andersen, O. K., et al.: Muffin-tin orbitals of arbitrary order. Phys. Rev. B **62**, R16219–R16222 (2000)
163. Löwdin, P.-O.: A note on the Quantum-Mechanical Perturbation Theory. J. Chem. Phys. **19**, 1396 (1951)
164. Ashcroft, N. W. and Mermin, N. D.: Solid State Physics. Saunders, Philadelphia (1976)
165. Skomski, R.: RKKY Interactions between nanomagnets of arbitrary shape. Europhys. Lett. **48**, 455 (1999)
166. Mattis, D. C.: Theory of Magnetism. Harper and Row, New York, (1965)
167. Skomski, R., et al.: Indirect exchange in dilute magnetic semiconductors. J. Appl. Phys. **99**, 08D504-1-3 (2006)
168. Dietl, T., et al.: Zener model description of ferromagnetism in zinc-blende magnetic semiconductors. Science **287**, 1019 (2000)
169. Priour Jr., D. J., et al.: A disordered RKKY lattice mean field theory for ferromagnetism in diluted magnetic semiconductors. Phys. Rev. Lett. **92**, 117201 (2004)
170. Coey, J. M. D., et al.: Ferromagnetism in Fe-doped SnO_2 thin films. APL **84**, 1332 (2004)
171. Das Pemmaraju, Ch. and Sanvito, S.: Ferromagnetism driven by intrinsic point defects in HfO_2. Phys. Rev. Lett. **94**, 217205, 1–4 (2005)
172. Venkatesan, M., et al.: Unexpected magnetism in a dielectric oxide. Nature **430**, 630 (2004)
173. Coey, J. M. D., et al.: Donor impurity band exchange in dilute ferromagnetic oxides. Nat. Mater. **4**, 173 (2005)
174. Griffin, K. A., et al.: Intrinsic ferromagnetism in insulating cobalt doped anatase TiO_2. Phys. Rev. Lett. **94**, 157204-1-4 (2005)
175. Zhang, J., et al.: Temperature-dependent orbital-moment anisotropy in dilute magnetic oxides. Phys. Rev. B **75**, 214417-1-5 (2007)

177. Antel, Jr, W. J., et al.: Induced ferromagnetism and anisotropy of Pt layers in Fe/Pt(001) multilayers. Phys. Rev. B **60**, 12933 (1999)
178. Janak, J. F.: Uniform susceptibilities of metallic elements. Phys. Rev. B **16**, 255 (1977)
179. Fulde, P.: Electron Correlations in Molecules and Solids. Springer, Berlin (1991)
180. Celinski, Z. and Heinrich, B.: Exchange coupling through Fe/Cu, Pd, Ag, Au/Fe Trilayers. J. Magn. Magn. Mater. **99**, L25 (1991)
181. Qi, Q.-N., et al., Strong ferromagnets: Curie temperature and density of states. J. Phys.: Condens. Matter **6**, 3245 (1994)
182. Mohn, P.: Magnetism in the Solid State. Springer, Berlin (2003)
183. Fischer, K.-H. and Hertz, A. J.: Spin Glasses. University Press, Cambridge (1991)
184. Kouvenhoven, L. and Glazman, L.: Revival of the Kondo effect. Phys. World, Jan., 33 (2001)
185. Kondo, J.: Sticking to my bush. J. Phys. Soc. Jpn. **74**, 1 (2005)
186. Madhavan, V., et al.: Tunneling into a Single Magnetic Atom: Spectroscopic Evidence of the Kondo Resonance. Science **280**, 567 (1998)
187. Li, J., et al.: Kondo scattering observed at a single magnetic impurity. Phys. Rev. Lett. **80**, 2893 (1998)
188. Újsághy, O., et al.: Theory of the fano resonance in the STM tunneling density of states due to a single kondo impurity. Phys. Rev. Lett. **85**, 2557 (2000)
189. Plihal, M. and Gadzuk, J.: Nonequilibrium theory of scanning tunneling spectroscopy via adsorbate resonances: Nonmagnetic and Kondo impurities. Phys. Rev. B **63**, 085404 (2001)
190. Cronenwett, S. M., et al.: A tunable Kondo effect in quantum dots. Science **281**, 540 (1998)
191. Manoharan, H. C., et al.: Quantum mirages formed by coherent projection of electronic structure. Nature **403**, 512 (2000)
192. Nilius, N., et al.: Tailoring electronic properties of atomic chains assembled by STM. Appl. Phys. A **80**, 951 (2005)
193. Giete, G. A., et al.: Kondo effect and STM spectra through ferromagnetic nanoclusters. Phys. Rev. B **66**, 024431 (2002)
194. Jamneala, T., et al.: Kondo Response of a single antiferromagnetic Chromium trimer. Phys. Rev. Lett. **87**, 25, 256804 (2001)
195. Madhavan, V., et al.: Observation of spectral evolution during the formation of a Ni_2 Kondo molecule. Phys. Rev. B **66**, 212411 (2002)
196. Wahl, P., et al.: Exchange interaction between single magnetic atoms. Phys. Rev. Lett. **98**, 056601(2007)
197. Schneider, M. A., et al.: Kondo state of Co impurities at noble metal surfaces. Appl. Phys. A **80**, 937 (2005)
198. Zhao, A., et al.: Controlling the Kondo effect on an adsorbed magnetic ion through its chemical bonding. Science **309**, 1542 (2005)
199. Fu, Y.-S., et.al.: Manipulating the Kondo resonance through quantum size effects. Phys. Rev. Lett. **99**, 256601 (2007)
200. Nielsen, M. A. and Chuang, I. L.: Quantum computation and quantum information. University Press, Cambridge (2000)
201. Burkard, G., et al.: Coupled quantum dots as quantum gates. Phys. Rev. B **59**, 2070 (1999)
202. Yao, W., et al.: Nanodot-Cavity quantum electrodynamics and photon entanglement. Phys. Rev. Lett. **92**, 217402 (2004)
203. Reimann, S. M. and Manninen, M.: Electronic structure of quantum dots. Rev. Mod. Phys. **74**, 1283 (2002)
204. Schofield, A. J.: Non-Fermi liquids. Contemporary Phys. **40**, 95 (1999)
205. Aharoni, A.: Introduction to the Theory of Ferromagnetism. University Press, Oxford (1996)
206. Kutner, R., et al.: Diffusion in concentrated lattice gases. II. Particles with attractive nearest-neighbor interaction on three-dimensional lattices. Phys. Rev. B **26**, 2967 (1982)
207. Skomski, R., et al: Ruderman-Kittel-Kasuya-Yosida interactions between spin distributions of arbitrary shape. J. Appl. Phys. **85**, 5890 (2000)

208. Mahadevan, P., et al.: Unusual directional dependence of exchange energies in GaAs diluted with Mn: Is the RKKY description relevant? Phys. Rev. Lett. **93**, 177201-1-4 (2004)
209. Michalski, S. A. and Kirby, R. D. unpublished (2007)
210. Smart, J. S.: Effective field theories of magnetism. Sunders, Philadelphia (1966)
211. Skomski, R., et al.: Superparamagnetic ultrathin films. J. Appl. Phys. **81**, 4710 (1997)
212. Das Sarma, S., et al.: Temperature-dependent magnetization in diluted magnetic semiconductors. Phys. Rev. B **67**, 155201 (2003)